J. Fluid Mech. (2014), *vol.* 756, *pp.* 771–815. © Cambridge University Press 2014
doi:10.1017/jfm.2014.453

Bursting water balloons

Hugh M. Lund[1,†] **and Stuart B. Dalziel**[1]

[1]Department of Applied Mathematics and Theoretical Physics, University of Cambridge, Wilberforce Road, Cambridge CB3 0WA, UK

(Received 25 January 2014; revised 25 January 2014; accepted 31 July 2014; first published online 4 September 2014)

The impact and rupture of a water-filled latex balloon on a flat, rigid surface is investigated using high-speed photography. Three distinct stages of the flow are observed, for which physical explanations are given. As the balloon lands and deforms, waves are formed on the balloon's surface for which the restoring force is tension in the latex. These waves are shown to closely obey linear potential theory for constant surface tension. Should the balloon rupture, a crack forms, from which the membrane retracts. Spray is simultaneously ejected from the water's surface, a consequence of a shear instability in the wake behind the retracting membrane. At later times, a larger-scale growth of the interfacial amplitude is observed, for which the generation mechanism is momentum in the water due to the preburst waves. However, it is argued that this is also a manifestation of the same mechanism that drives Richtmyer–Meshkov instability (RMI). Further, it is shown experimentally that this growth of the interface may also occur when there is no density difference across the balloon, a situation that does not arise for the standard RMI. An analytical model is then derived to predict the interfacial growth for such an interface, and is shown to predict the asymptotic growth rate of the interface accurately.

Key words: instability

1. Introduction

Filling up a balloon with water and then throwing it at something (or someone) is a game enjoyed by children both young and old throughout the world. The reason for this popularity is simple: water balloons allow a large amount of water to be accurately delivered to a target over distances of several metres, without the need for a high-speed jet. At first glance, the process would appear straightforward; the rubber membrane stretches as it fills, before being tied up to prevent water escaping. The membrane then keeps the water together as it moves through the air towards its target, before breaking up as it deforms on impact. The water then spreads out over the target, covering it in water. This simple explanation shows why it is popular with children, but not why it is of interest to scientists. Yet within this apparently simple process lies a wealth of complicated physics that, thanks to modern high-speed imaging, can now be observed. Many such videos can be found on the Internet, with a simple search of the video-sharing website Youtube revealing videos of water

† Email address for correspondence: hugh.lund@gmail.com

https://doi.org/10.1017/jfm.2014.453 Published online by Cambridge University Press

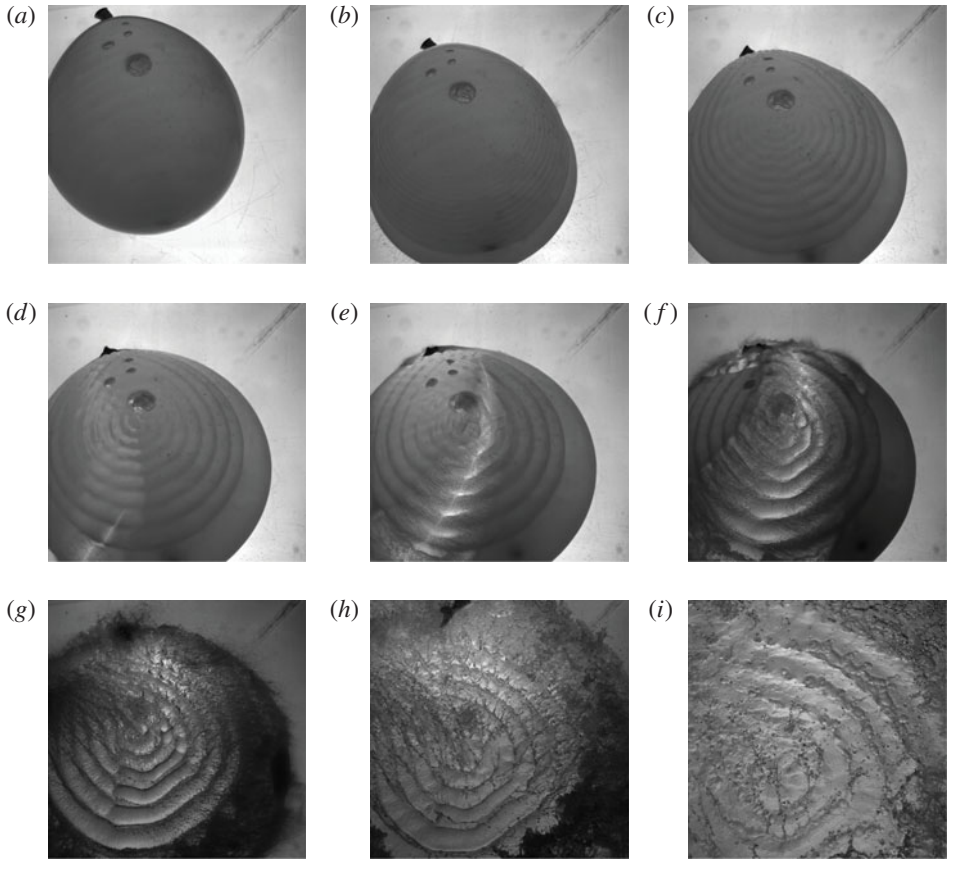


FIGURE 1. The behaviour of a 300 mm diameter water balloon upon impact with a rigid surface: (*a*) $t=-6$ ms; (*b*) $t=7$ ms; (*c*) $t=11$ ms; (*d*) $t=13$ ms; (*e*) $t=14$ ms; (*f*) $t=15$ ms; (*g*) $t=20$ ms; (*h*) $t=31$ ms; (*i*) $t=58$ ms. The first image is taken approximately 500 ms after the balloon was released, by hand, from a height of 1 m.

balloons bouncing, bursting, or both, on a wide range of surfaces (see supplementary movie 1 available at http://dx.doi.org/10.1017/jfm.2014.453). These videos may garner hundreds of thousands of views, demonstrating that even the small-scale details of a bursting water balloon fascinate many of us.

However, despite this evident public interest, no evidence of serious scientific research into this process can be found in the literature. Consequently, our initial motivation for this research was not the published work of others, but some basic experiments doing exactly what has just been described: dropping a water balloon onto a rigid surface. Consequently, we first describe one such experiment in detail.

In the sequence of images shown in figure 1, a full water balloon is dropped onto a rigid surface, causing it to burst. The balloon is what may be regarded as a standard party balloon, with a maximum diameter when fully inflated of 300 mm; it was dropped from a height of 1 m, bursting on impact. The whole process was captured using a high-speed camera recording at 5400 f.p.s. Further description of the equipment used is given in § 2, but the specifics are not important here as we wish to give only an overview of the problem.

https://doi.org/10.1017/jfm.2014.453 Published online by Cambridge University Press

Instead, we give a brief description of what is occurring in each image as follows (times are all accurate to the nearest millisecond, with $t = 0$ ms being the moment of first contact between the balloon and rigid surface).

(*a*) The balloon is in free-fall. A fully inflated balloon with no density difference between the fluids inside and outside is approximately pear-shaped due the way it was made. When in free fall, the balloon inflated with water also assumes this shape, as gravity can no longer influence the shape. This is distinct from its sessile shape, the shape it formed when full of water but resting on a flat surface. Water is added through a small opening that is tied once the balloon is full: the knot is visible near the top of the image. As the balloon was released by hand, there is likely to be a rotational element to its motion, although this is insignificant compared with its downward speed. The deformation of the balloon, when held prior to release, likely created small-amplitude waves on the membrane, although these have died away by now to the extent that they are not visible. Small bubbles of air may be viewed inside the balloon near the top of the membrane, an unfortunate artifact of the filling of the balloon directly from a tap. In later experiments requiring quantitative measurements, this problem was alleviated by filling the balloon when completely submerged in water; here, it suffices to say that such bubbles did not have any significant qualitative effect on the experiment.

(*b*) The balloon starts to deform shortly after initial impact with the tank floor. First contact with the tank occurs at $t = 0$ ms, causing the surface to flatten. Waves of a wide range of wavenumbers are created on the elastic membrane, with the short wavelengths travelling faster. Here, soon after the initial impact, only relatively short waves are seen, with wavelengths around 1 mm. No shorter wavelengths are seen, as they have been suppressed by the bending stiffness of the membrane and were the waves most strongly affected by dissipation. The shape of the wavefronts approximately follows the pear-like shape of the balloon.

(*c*) The balloon continues to deform due to the tank floor. At this later time ($t = 11$ ms), the shorter waves seen earlier have reached the top of the balloon, reflected and undergone significant decay. Now, it is the larger-wavelength, larger-amplitude waves that are seen; the wavelengths are of the order of centimetres. As before, the waves travel from bottom to top of the balloon, although at a slower rate than those with shorter wavelengths. By now, the shape of the balloon no longer approximates a pear, becoming flatter as it spreads out over the tank floor. Consequently, the total surface area of the balloon has increased, despite the volume within it remaining fixed.

(*d*) The balloon continues to spread out, with the waves seen in the previous images still present at $t = 13$ ms. However, the further increase in surface area and consequent increase in stress within the elastic membrane has caused it to fail at a point out of view on the underside of the balloon. This has led to a crack (seen near the bottom of the image) propagating through the elastic membrane. Either side of the crack, the membrane starts to retract away from the initial position of the crack.

(*e*) Over only a millisecond, the crack has taken a curved path across nearly half the membrane. While the waves seen earlier persist away from the crack, much of the elastic membrane is now in retraction. Behind the retracting membrane, water is being ejected from the surface as a small length-scale spray.

https://doi.org/10.1017/jfm.2014.453 Published online by Cambridge University Press

(*f*) One millisecond later at $t = 15$ ms, the crack has now spread round the whole membrane, deviating significantly from its initial path as it nears the tied end of the balloon. Most of the membrane is now in retraction; the fine spray from the water's surface is now seen everywhere away from the path of the crack. This spray is water ejected from the main body of water previously within the balloon that travels upwards with a slight lean in the direction to which the membrane is retracting. This spray has a characteristic length scale of the order of tenths of millimetres. Throughout the short time the crack was propagating (around 3 ms), the larger preburst waves persisted wherever the membrane was still present, with the balloon as a whole continuing to flatten and spread out.

(*g*) At $t = 20$ ms, the water surface is now almost completely uncovered by the membrane. The full retraction of the membrane from the initial formation of the crack took around 8 ms. Some of the fine spray seen in images (*e*) and (*f*) remains, although mainly near the edge of the water, where the membrane was last to retract. Elsewhere, larger-scale undulations in the water's surface are clearly visible; the undulations have approximately the same shape and wavelength as the preburst interfacial waves.

(*h*) The water has spread out and thinned significantly by $t = 37$ ms, while the fine spray has now almost disappeared. This has been replaced by thin crown-like structures of the same wavelength as the preburst waves. These crowns are propagating upwards into the air, with the water surface between them approximately flat. These structures are thin sheets of water that are almost axisymmetric away from their leading edge; this axisymmetry is lost near the leading edge, where they break up into small droplets due to capillary forces.

(*i*) Much later, at $t = 58$ ms, gravity has come to dominate the flow. This has caused the fine spray and crown-like structures to retract back into the main body of water, which is now spread thinly over the tank floor. The dominant motion of the water is now radially outwards from where the balloon landed, although the remains of the crowns are still visible. After this image, the water continues to spread until it reaches the tank walls. It then sloshes around until finally coming to rest as a thin, flat layer over the tank floor.

It is easy to see from this description of just one experiment that the drop and consequent burst of a water balloon involves a complex range of non-trivial physical phenomena. As stated earlier, no known research has been published to examine this situation, and little on fluid-filled balloons in any situation.

Detailed, quantitative study of these phenomena for a dropped water balloon in air proved impossible, however. The experiment involved a large number of unknowns, including where the balloons would land, in what orientation, and when exactly they would burst. Little, too, was known about the balloons themselves, as they had simply been purchased straight from a commercial retailer. The experiments were thus unrepeatable. Consequently, we first describe in § 2 a different experimental method we have developed.

The whole process may be considered as three distinct stages of interest. Tension-driven waves were observed on the membrane after impact but before rupture, and are discussed in § 3. Should the membrane rupture, it then retracted rapidly, leading to a 'spray' being ejected from the water, a process discussed briefly in § 4. If tension-driven waves were present on the membrane at the moment of rupture, a late-time growth of the interfacial amplitude was seen. This growth was the main focus of our research, and is discussed in detail in § 5. In § 6, a model is derived for the

https://doi.org/10.1017/jfm.2014.453 Published online by Cambridge University Press

nonlinear stages of growth when a water-filled balloon with tension-driven waves on the membrane is ruptured underwater. Any literature related to each stage will be discussed in the relevant section.

2. Improved experimental method

A significantly improved experimental method was developed in response to the issues described in the introduction, through which all of the significant physical phenomena discussed previously could be quantitatively observed. Instead of dropping the balloons, they were oscillated while held stationary, before being ruptured with a sharp object. This allowed us to isolate and examine each of the three main stages separately, and permitted accurate measurements of the flow to be taken from images captured on a high-speed camera. With the exception of irregularities in the membranes themselves, all of the issues raised previously were mitigated significantly. This method also worked when the balloons were submerged in water, permitting us to study the behaviour of perturbed and burst balloons when there was no density gradient across the membrane or post-rupture surface tension.

2.1. *Balloons*

For all of the following experiments, the balloons used were made from natural rubber, also known as latex. All of the balloons used were sold as being 130 mm in diameter when fully inflated, although for our experiments they were inflated to a diameter between 80 and 140 mm. This is in contrast to the most commonly available size of balloon (as used in figure 1), that has a maximum diameter nearer 300 mm. Using the smaller balloons was a necessity, due to the scale of the rest of the equipment. Quasi-static inflation and deflation tests did find evidence of the Mullins effect (Mullins 1969), whereby the stress–strain relation for the balloon changed depending on the number of previous inflations. To ensure greater consistency in the stress–strain behaviour between different balloons, all of the balloons were fully inflated and deflated once, prior to their use in any oscillation and rupture experiment. The uninflated thickness of the balloons varied over their length, but was typically around 0.16 mm (after being inflated then deflated once) in the main, spherical section that we were most interested in. Although difficult to determine accurately from a balloon, our best estimate of the rubber's density was 976 kg m^{-3}, in good agreement with the value of 970 kg m^{-3} given for natural rubber by Mark (2009).

2.2. *Equipment set-up*

The experimental lay-out is given in figure 2. Experiments were conducted with both air and water external to the balloon. The non-dimensional density difference across the membrane is given by the Atwood number

$$A = \frac{\rho_{in} - \rho_{out}}{\rho_{in} + \rho_{out}} \tag{2.1}$$

where ρ_{in} is the density of the fluid within the balloon, and ρ_{out} is the density of the fluid outside the balloon. For the air/water case, $A \approx 1$, whereas for the water/water case, $A = 0$. Prior to each experiment, the balloon was attached to the end of a 6 mm diameter plastic tube, before water was poured down a 1500 mm long, 14 mm diameter tube held vertically and attached to the other end of the 6 mm tube. The

https://doi.org/10.1017/jfm.2014.453 Published online by Cambridge University Press

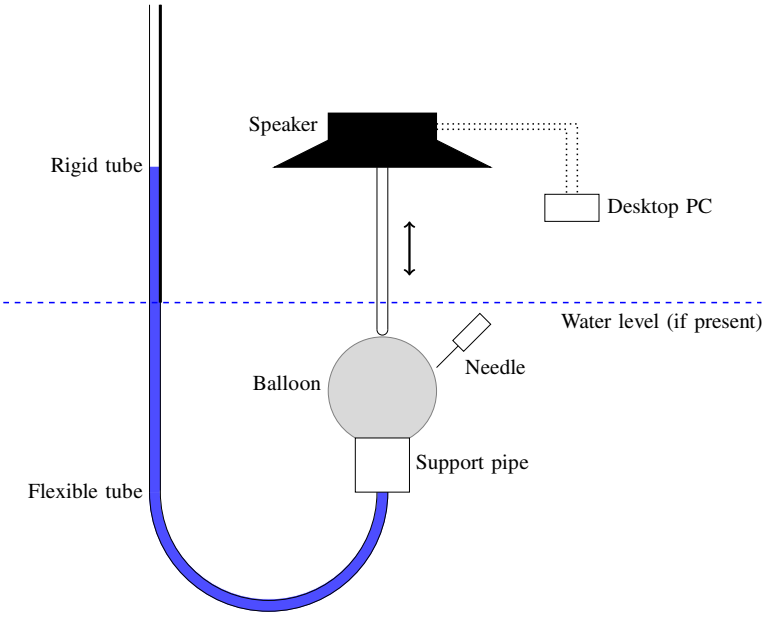


FIGURE 2. (Colour online) The experimental set-up used to oscillate 130 mm balloons at a fixed frequency before they were ruptured by the needle.

pressure within the balloon was then calculated by assuming it was in balance with the hydrostatic pressure within the 14 mm tube. When the experiment was being conducted with air external to the balloon, the height of the water column was measured from the centre of the balloon; with water external to the balloon, the height of water column was taken from the surface of the water within the tank. From these pressure measurements, the tension within the balloon was estimated using the Laplace–Young equation for a spherical interface

$$\Delta p = \frac{2\sigma}{R}, \tag{2.2}$$

where Δp is the pressure difference across the interface, R is the radius of the (approximately) spherical filled balloon and σ is the tension within the balloon.

In addition, the balloon was supported by a section of 60 mm diameter pipe that helped to support it when fully inflated. This support pipe restricted the overall movement of the balloon when oscillated, helping to ensure that its centre remained approximately stationary. However, where the balloon was in contact with the pipe, the displacement of the balloon was fixed at zero, and so the presence of the support pipe did play a role in setting the resonant modes of oscillation.

To explore the post-rupture response of the tension-driven waves we observed on the dropped balloon prior to rupture, the balloon was subjected to periodic forcing before being deliberately ruptured. This forcing was achieved using a 70 W loud speaker with an impedance of 8 Ω and polypropylene cone of diameter 200 mm. A cut-away plastic beaker had been glued to the speaker, with a 350 mm long rigid rod firmly attached to the beaker. The whole apparatus was then suspended approximately 500 mm above the tank floor. An analogue output card installed in a computer was used to drive the position of the speaker via an 80 W audio amplifier. A balloon

https://doi.org/10.1017/jfm.2014.453 Published online by Cambridge University Press

was then put in place and filled as described above, and the speaker adjusted so that the rod was aligned with the balloon's axis of symmetry and in contact with the top of the balloon (see figure 2) such that it created a static deformation in the surface approximately 10 mm in depth, to ensure that it remained in contact with the balloon for as greater part of the period of oscillation as possible. Once the balloon was in position, the frequency of oscillation and output voltage from the analogue output card were chosen, and the speaker activated. The balloons were then forced at the requisite frequency for at least 1 s to ensure only waves of the correct frequency were present on the balloon.

The experiments were all performed within the same transparent acrylic tank with base 0.6 m $\times$ 0.6 m and height 0.45 m. They were recorded at 1 MP resolution using a Photron Fastcam SA1.1 high-speed video camera, operating at either 2000 f.p.s. or 5400 f.p.s. In some experiments, the water inside the balloon was dyed with either milk powder or disodium fluorescein to allow the motion of the interface after rupture to be easily tracked; from such experiments, the wavelength and amplitude of the interfacial waves could be determined. For information about the rest of the flow, it was necessary to perform particle image velocimetry (PIV). For this, approximately neutrally buoyant 180–212 μm Pliolite particles were used, after being mixed with rinse aid to overcome their hydrophobic nature. A number of such particles were then poured into the balloon, the water outside (if present), or both. The experiments were illuminated using a 700 W arc lamp projecting light through a slit formed on the tank's side using two blackened metal strips and black, self-adhesive film. After the images had been saved to hard-disk, they were analysed using the PIV facility within the program DigiFlow. The velocity and vorticity of the flow was then determined with a resolution of one measurement per 4 mm^2. We note that the measured vorticity created by the preburst waves was in approximate agreement with the theory outlined in § 3.

There were, ultimately, three free input parameters that we could vary: the output voltage that determined the amplitude of the oscillations of the rod, the volume of the balloon (and, hence, tension in the membrane), and the oscillation frequency f. As we were not investigating the consequences of changing the wave amplitude, the output voltage was kept constant at 0.8 V throughout. The remaining two parameters were limited in range by the experimental equipment available to us. The volume was limited at the lower end by the need to have waves of a sufficient wavelength and amplitude (while remaining linear) to enable good flow visualisation, and at the upper end by the likelihood of spontaneous bursting of the balloon. The input frequency was limited at the lower end by the appearance of higher harmonics in the forcing below 50 Hz, and at the upper end by the power of forcing available: the greater the frequency of forcing, the smaller the amplitude, limiting forcing to frequencies under 180 Hz.

3. Preburst waves

For a water-filled balloon dropped in air, waves appeared on the membrane during the deformation of the balloon after impact. Detailed modeling of the interfacial waves created upon impact was difficult, as the deformation of the balloon made the geometry complicated, and led to significant changes in the tension in membrane. These problems were overcome by the experimental method described in § 2. In both cases, however, the physics of the waves was clear: the restoring force for these waves was tension within the membrane, which acted to minimise the surface area of the balloon.

https://doi.org/10.1017/jfm.2014.453 Published online by Cambridge University Press

For the dropped balloons, it was waves travelling up the membrane that were seen as the balloon landed and deformed. Similarly, with the held and oscillated balloons, when the forcing began it was travelling waves that were seen. However, after a few oscillations, the travelling waves created by the oscillated rod combined with those reflected from the supporting tube to form a steady interference pattern, so that standing waves were seen. It should be noted that failure to oscillate at a resonant frequency, along with dissipation causing the reflected upward-travelling waves to have smaller amplitude that those travelling downwards, did cause some travelling waves to persist. However, these travelling waves were negligible in their impact, serving only to create a small amplitude modulation to the dominant standing wave pattern. For the range of parameters used in our experiments, the time for a single wave to travel to the bottom of the balloon and back up again, was between 0.05 and 0.15 s. For times larger than this, the perturbations on the interface were effectively standing waves. In all experiments with oscillated balloons, the oscillations were started at least 1 s before measurements were taken, to ensure only standing waves were seen. There was the potential for some beating of the standing waves to occur: if the oscillation frequency was not an exact resonant frequency, the interference pattern would not be steady (so that the position of nodes was fixed) but instead would oscillate position. Similarly, dissipation would also mean that the waves were not perfect standing waves. However, no significant variation of the position of nodes was observed experimentally, so that the interfacial waves could be approximately regarded as steady standing waves.

The wavelength λ of the interfacial waves varied between 10 and 100 mm, while the amplitude $\tilde{A}$ of the waves lay in the range 1–10 mm. For a spherical interface, a linear wave is one for which the amplitude of the wave is much smaller than both their wavelength and the radius of the sphere R. In our experiments, R lay between 40 and 60 mm, clearly giving $\tilde{A}/R \ll 1$ for all of the experiments. It was also true that $\tilde{A}/\lambda \ll 1$ in every experiment, as our choice of experimental equipment meant that $\tilde{A}$ and λ were not independent: increasing the frequency of forcing (and thus decreasing the wavelength) led to a corresponding decrease in the maximum available forcing amplitude (and, thus, that of the waves). Consequently, the waves in all our experiments could be regarded as linear.

As a further consequence of the linearity of these waves, the relative change in surface area was small: with the amplitude around a tenth of the wavelength, the change in surface area was around 1 %. This, in turn, meant that the balloon was never perturbed far from its initial, near-spherical shape, and the tension in the latex membrane was essentially unaffected by the waves.

3.1. *Linear theory*

We model the preburst waves using linear theory. As discussed above, this was an accurate assumption for the waves created using the forced oscillation. Note, however, that this was not the case for some of the wave modes seen on a dropped water balloon, where the distortion of the balloon was anything but small. Yet it was approximately true for many such waves, and as figure 1 revealed, the presence of linear waves on the interface at rupture did lead to interfacial growth. To simplify the derivation of the theory, we make several further assumptions: that the water is incompressible (a common assumption), the balloons are spherical (a reasonable assumption when considering only the section away from the open end), and that the flow is of high Reynolds number and axisymmetric. We could reasonably attempt to

https://doi.org/10.1017/jfm.2014.453 Published online by Cambridge University Press

model the flow by assuming it to be inviscid, but as will be revealed later, doing so misses some significant behaviour related to the interaction between the flow and the balloon. For the balloons forced at a single on-axis point, deviations from axisymmetry of the flow will only arise from non-axisymmetry of the balloon. For dropped balloons, the non-sphericity of the balloons means that their orientation upon impact will affect the axisymmetry of any waves created; any horizontal motion of the balloon through the air may also have the same effect.

We consider here only capillary waves. While gravity clearly plays a role in generating the waves on a dropped balloon, causing its acceleration through the air, tension in the membrane will be the dominant restoring force as they propagate, for all but the few waves of greatest wavelength. We also neglect bending stiffness of the membrane, as it will be negligible for waves of wavelength much greater than the membrane thickness $h = 0.16$ mm. For oscillated balloons, only waves of a single frequency and therefore wavelength were formed in each experiment. The shortest of these waves had a wavelength of the order of 10 mm, so bending stiffness was always unimportant. For the dropped balloons in air, the impact of the balloon created waves on the full spectrum of frequencies, and therefore wavelengths. The bending stiffness would therefore play a significant role in limiting the amplitude of the waves of shortest wavelength. The following analysis should therefore only be regarded as accurate for waves of wavelength over 1 mm.

We are therefore left to solve the inviscid linear Navier–Stokes equations in spherical coordinates (r, θ, ϕ), neglecting all motion in the θ (azimuthal) direction, subject to regularity conditions at $r = 0$ and ∞, and coupled with equations for the motion of the rubber membrane. As the membrane is so thin, we may neglect shear motions and stresses within it. It may therefore be modelled as a fluid interface, with its influence on the fluids either side captured through the application of interfacial conditions on the fluids at $r = a$, the undisturbed radius of the balloon. These interfacial conditions are continuity of velocity and stress; as we are considering viscous fluids, this applies in the directions both normal and tangential to the interface.

Classical theory of capillary waves concerns flow near a pure fluid–fluid interface. A water balloon, whether in air or underwater, is clearly not a pure fluid–fluid interface. There are a great number of similarities, yet also some significant differences. These differences arise because for a pure fluid–fluid interface, only a constant surface tension acts – the surface itself is free to expand and contract without change in the magnitude of the interfacial tension. For an interface covered in rubber, this is clearly not true: stretching the membrane will cause the tension in it to increase significantly. Such gradients in tension will act to limit the tangential motion of the interface. The relevant theory has received much attention, due to the way oil slicks on an ocean surface may act as a thin elastic interface (that this theory is equally applicable to an actual elastic membrane has been noted by Christensen (2005), amongst others). A useful summary is given by Christensen (2005), while a complete review is given by Lucassen-Reynders & Lucassen (1969). When the stress required to expand or contract the membrane is far less than shear stresses in the fluid, the effect of the membrane on the flow is negligible, and the interface may be regarded as a pure fluid–fluid interface. Consequently, the interfacial area may change significantly during a single wave period. When the stress required to expand or contract the membrane is far greater than shear stresses in the fluid, the influence of the membrane becomes significant and the interface is referred to as inextensible, acting as something akin to a rigid boundary. The relevant importance of the two stresses is measured by the

https://doi.org/10.1017/jfm.2014.453 Published online by Cambridge University Press

non-dimensional parameter given by Christensen (2005),

$$\mathcal{E} = \frac{\tilde{E}k^2}{\nu^{1/2}\rho\omega^{3/2}}, \tag{3.1}$$

where ρ is the density of the fluid, ν its kinematic viscosity, k the wavenumber, ω the angular frequency of oscillation, and $\tilde{E}$ the gradient of the stress–strain relationship in the membrane. For $\mathcal{E} < 1$, the fluid stresses are dominant; for $\mathcal{E} > 1$, stresses in the membrane are dominant. In the limit $\mathcal{E} \to \infty$, the interface is regarded as inextensible; the greater stress in the membrane suppresses all tangential motion at the interface. For the waves created by our forced oscillations, typical values were $\mathcal{E} \approx O(10^2) \gg 1$, and thus our balloon interface may be regarded as inextensible.

The model we have described above, for linear waves on an inextensible spherical interface, has been considered before by other authors, so we shall not provide any derivation here. While it was Lamb (1932) who first considered an inextensible air/water interface in two dimensions, it was Miller & Scriven (1968) who went further and derived the dispersion relations for both planar and spherical inextensible interfaces with two fluids of non-negligible viscosity and density. Note, however, that their work appears not to have been applied to actual membrane-covered interfaces, let alone water-filled balloons, anywhere in the literature.

For any fluids, the shape of the interface (and other flow quantities) may be written as the sum over (dimensionless) wavenumber k of spherical harmonics $P_k(\cos(\phi))$, where P_n represents the Legendre polynomial of degree n. As a consequence of this, for waves of a single wavenumber as in our forced oscillation experiments, the amplitude of the waves is not constant around the interface; the amplitude of the waves is greatest nearest the poles, and monotone decreasing as the mid-point $\phi = \pi/2$ is approached. The same is true for other flow quantities, such as velocity, and the circulation created by the waves at the interface.

We consider in detail the two cases most relevant to our experiments: inextensible air/water interfaces, and inextensible water/water interfaces. The air/water case may be simplified by assuming that the density of the fluid outside the membrane may be neglected. Consequently, the external fluid provides no tangential stress and only a constant normal stress to the membrane (what is referred to as a free surface for such a pure fluid–fluid interface). In both cases, the relevant Reynolds numbers for the flow will be in excess of $Re \approx 10^3$. An alternative Reynolds number based on the circulation within one half-wavelength at the moment of rupture Γ, $Re_\Gamma = \Gamma/\nu$, is also of the order 10^3. The viscosities of the fluids involved will therefore be small relative to the inertia of the fluids, and so the kinematic viscosity of water, ν, may be considered a small parameter. To leading order in ν, the theory predicts the angular frequency of oscillation ω to be

$$\omega = \sqrt{\frac{\sigma k(k-1)(k+2)}{a^3\rho}} \tag{3.2}$$

for an inextensible air/water interface, as found by Miller & Scriven (1968). Here, σ is the (constant) undisturbed tension within the membrane, a is the undisturbed radius of the balloon, ρ the density of water and k the (dimensionless) wavenumber. For a water/water interface, the leading-order term given by Miller & Scriven (1968) is

$$\omega = \sqrt{\frac{\sigma k(k+1)(k-1)(k+2)}{a^3\rho(2k+1)}}. \tag{3.3}$$

https://doi.org/10.1017/jfm.2014.453 Published online by Cambridge University Press

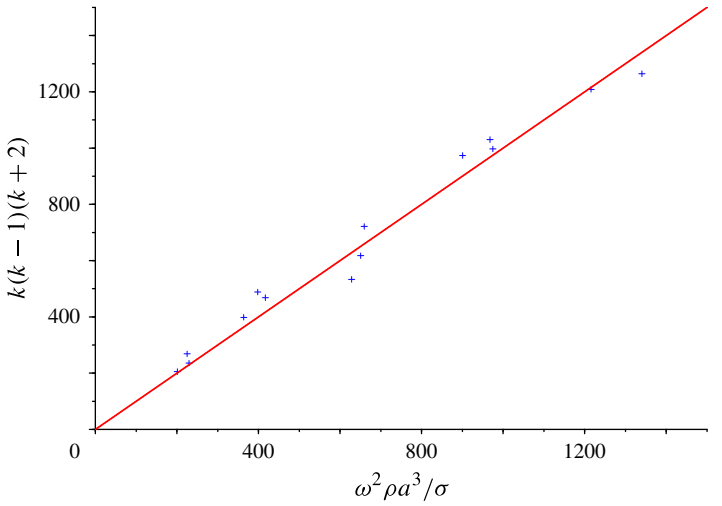


FIGURE 3. (Colour online) The relation between σ, ω and k for water-filled balloons held and oscillated in air ($\rho = 1000$ kg m^{-3}). The tension σ was derived using the method given in § 2.2, with the wavenumber k determined by counting the number of waves around the balloon. Displayed is the experimental data (marks, blue online) and the theoretical prediction of (3.2) (line, red online).

Note that these frequencies match those for a pure fluid–fluid spherical interface, as first found by Rayleigh (1879) and Lamb (1932), respectively.

Experimental confirmation of these dispersion relations in the membrane-covered cases is given in figures 3 and 4, for the two cases of air and water external to the membrane, respectively; there is no evidence in the literature of any such experiments, measuring the properties of surface waves on water-filled balloons, having been done before. The error for each experiment is estimated at ± 50 rad^{-1}. It is clear that here, our experimental data closely fits the theoretical predictions of (3.2) and (3.3). This suggests that our use of a linear model is correct, as a first approximation. The quality of this fit is not affected by introducing the first-order viscous correction to the oscillation frequency, as found by Miller & Scriven (1968). As the viscosity of water is so small, any changes to oscillation frequency introduced by viscosity are so small as to be insignificant in comparison with the inviscid approximation. The finite size of the tank also does not influence these results, as flow velocities decay like $(a/r)^{k+1}$ outside the balloon. The walls were typically at a distance 0.4 m (so a non-dimensionalised distance $r/a = 0.4/0.05 = 8$) from the balloon, implying typical velocities near the walls a factor $(0.05/0.4)^{11} \approx 10^{-10}$ smaller than at the interface. Consequently, the no-flow conditions at the tank walls were approximately satisfied, and thus had no impact on the flow near the balloon.

From these first-order approximations to the frequency, we may estimate the phase speed of waves, $c_p = \omega/k$. In particular, for an air/water interface,

$$c_{p_{air}} = \sqrt{\frac{\sigma(k-1)(k+2)}{ka^3\rho}}, \tag{3.4}$$

https://doi.org/10.1017/jfm.2014.453 Published online by Cambridge University Press

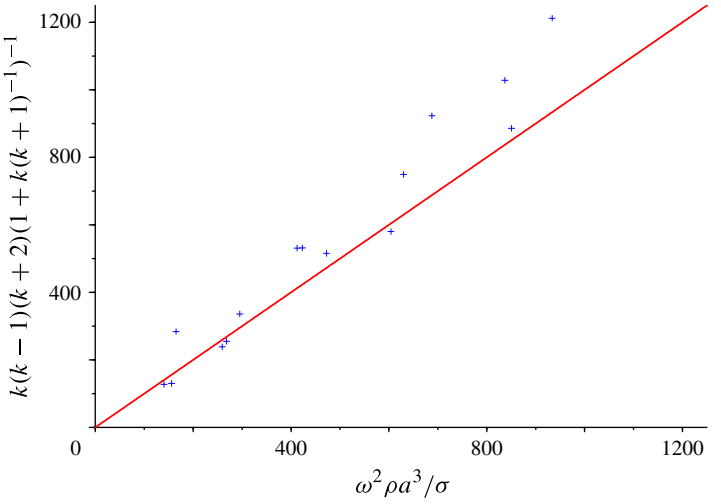


FIGURE 4. (Colour online) The relation between σ, ω and k for water-filled balloons held and oscillated underwater ($\rho_2 = \rho_1 = 1000$ kg m^{-3}). The tension σ was derived using the method given in § 2.2, with the wavenumber k determined by counting the number of waves around the balloon. Displayed is the experimental data (marks, blue online) and the theoretical prediction of (3.3) (line, red online).

and for a water/water interface

$$c_{p_{water}} = \sqrt{\frac{\sigma(k+1)(k-1)(k+2)}{k(2k+1)a^3\rho}} = \sqrt{\frac{k+1}{2k+1}}c_{p_{air}}. \tag{3.5}$$

For all $k > 1$ these phase speeds are monotone increasing in k. Although the expression is more complicated, the same is true for the group velocities $c_g = \partial\omega/\partial k$.

This increase in wave velocity with k implies that high wavenumbers travel fastest, or equivalently that short waves travel fastest. This was noted by Lamb (1932) for true capillary waves, and explains our observations from § 1 that it is the shorter waves that are visible first when a dropped balloon impacts a rigid surface: waves of all wavenumbers are created at the moment of impact, but it is the shortest ones that travel up the balloon fastest, and thus become visible first.

It is easy to see from the above analysis how the tension was acting very much like the surface (capillary) force of a liquid. The capillary-like nature of these interfacial waves suggests a clear analogy with capillary waves on a fluid droplet. Richard & Quere (2000) studied the impact of water droplets on a hydrophobic surface, with the behaviour of the droplets closely mirroring that of water-filled balloons that do not rupture on impact. In both cases, the initial gravitational potential energy was converted into kinetic energy as it accelerated downwards. Upon impact, the balloon or droplet deformed, flattening and spreading over the surface as capillary waves travelled from the point of impact to the top. At the same time, kinetic energy was converted into either elastic potential energy for the balloon or surface energy for the droplet. The balloon or droplet would then continue to expand before high pressures near the outer edge accelerated the fluid there inwards, causing it to retract and lift off the surface once more, as the surface energy was converted back into kinetic energy.

https://doi.org/10.1017/jfm.2014.453 Published online by Cambridge University Press

It was, therefore, the tension in the balloon when filled and stationary that determined the oscillation frequency of the waves; the elasticity of the membrane (manifested through the change in tension with stretch) therefore played no significant role. The membrane elasticity did, however, affect the decay rate of the waves. For a pure fluid/fluid air/water interface, Miller & Scriven (1968) give the typical decay time of the waves, at the scale of our experiments, as

$$\tau = \frac{a^2}{(2k+1)(k-1)\nu} \approx 53 \text{ s}. \tag{3.6}$$

This should be contrasted with the much faster decay

$$\tau = \frac{2\sqrt{2}\rho^{1/2}a^{5/2}(k+1)}{(k-1)^{5/2}k^{1/2}(k+2)^{1/2}\sigma^{1/2}\nu^{1/2}} \approx 1.5 \text{ s} \tag{3.7}$$

for an inextensible air/water interface at this scale. The decay rate proportional to ν seen in (3.6) is associated with viscous decay in the outer flow, away from the interface. Such terms are therefore present in all flows, whatever the form of the interface. The (greater) decay rate proportional to $\nu^{1/2}$ seen for an inextensible interface in (3.7), is associated with the flow in the interfacial boundary layer. For a water/water interface, the decay time is around 1.1 s whether or not the membrane is present, as symmetry between the phases means that the fluid the other side of the interface provides resistance to tangential motions even when the membrane is not present. Note that decay proportional to $\nu^{1/2}$ mirrors that seen in a viscous boundary layer on a solid wall (see Batchelor 1967, p. 311).

As will be discussed in § 5, the distribution of vorticity at the moment of rupture may play an important role in the nonlinear stages of the late-time interfacial growth. The vorticity is concentrated in boundary layers of thickness $\sqrt{2\nu/\omega} \approx 0.1$ mm on either side of the interface. Note that this is far smaller than the typical wavelength of the preburst waves (around 10 mm), thus it is appropriate to assume the vorticity is contained within a vortex sheet on the interface. This is supported by our PIV experiments (for example figure 5), where the vorticity is clearly seen to be concentrated in a thin layer near the interface. The total circulation density (that is, the vorticity integrated in the direction normal to the interface) is the same whatever the two fluids. Exactly where the vorticity is located does depend on the fluids, and the nature of the interface, however, as discussed by Craik (1985). For either membrane-covered interface, the inextensibility of the membrane means that the vorticity is (approximately) equally split between the phases, with the circulation density order 1 in the kinematic viscosity ν on both sides. However, for an uncovered air/water interface, the circulation density is only order ν in the water, but order $\nu^{1/2}$ in the air. This is because the difference in densities means that motion in the air provides little resistance to motion in the water, but the motion in the water provides significant resistance to motion in the air. The shear between the outer flows is therefore primarily located in the air. This distinction will be important when discussing the late-time growth of the interfacial amplitude, in § 5.

4. Rupture and retraction of the membrane

The second stage observed in the bursting of a water-filled balloon was the rupture of the balloon, and consequent instability on the fluid–fluid interface. One example

https://doi.org/10.1017/jfm.2014.453 Published online by Cambridge University Press

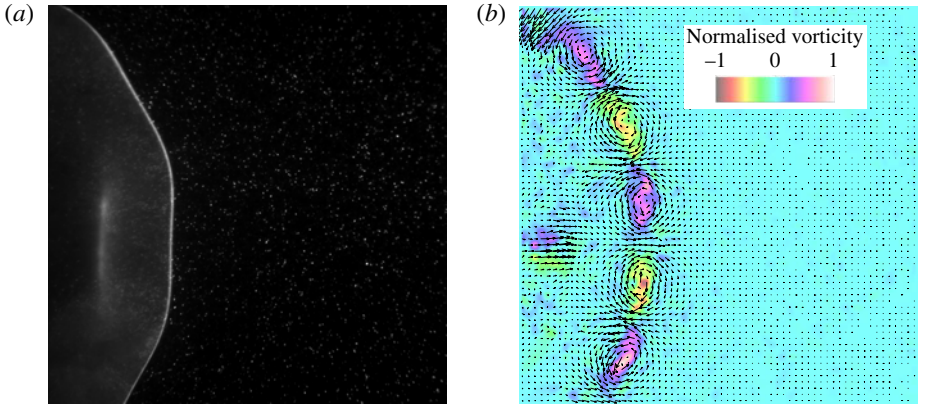


FIGURE 5. (Colour online) The flow field created by a water-filled 130 mm membrane oscillated underwater at 105 Hz over one forcing period: (*a*) $t = 0.0$ ms; (*b*) $t = 2.5$ ms. (*a*) The set-up used, with particles both inside and outside the membrane and a light sheet shone vertically through it. (*b*) The results of PIV performed on the resulting video, with the arrows representing the velocity field and the colours representing the vorticity: purple for positive vorticity, cyan for zero, green for negative. The scale given is dimensionless, with all values scaled by the maximum magnitude of vorticity in the sequence.

of the behaviour for a balloon with water both inside and outside the membrane is given in figure 6. When the pin first penetrates the membrane, a small hole is formed, as seen in figure 6(*a*). Tension in the membrane then pulls the (stress-free) faces of this hole apart, leading to the propagation of a crack. Figure 6(*b*) shows how, only 0.7 ms after the first penetration, the crack has spread both upwards and downwards, and is now approximately half way round the balloon's circumference. Small wave-like perturbations are also seen on the water/water interface behind the retracting membrane. These perturbations are much clearer 1.2 ms later in figure 6(*c*), when the crack has spread nearly three-quarters of the way round the balloon. Waves of a similar wavelength and amplitude may also be seen on the membrane, near the free edge. Finally, 4.3 ms after rupture was initiated, figure 6(*d*) shows the membrane fully retracted and beginning to buckle. The perturbations to the water/water interface are still visible, but while those near the membrane are wave-like, the region near the initial crack propagation path appears turbulent. While it may argued that this region is instead experiencing 3D wave perturbations of varying scales, our argument in favour of turbulence is supported by the Reynolds number for the flow created by the retracting membrane being $Re \approx 10^3$, which is on the boundary of transition to turbulence for flow past a flat plate.

4.1. *Rupture of the membrane*

Rupture of the balloon was initiated by the propagation of one or more mode I (or opening) cracks through the membrane. For the dropped balloons, the higher tension created by its expansion over the tank floor caused a crack to begin from a flaw in the membrane; for the oscillated balloons, the crack began from where the membrane was pierced by the pin. Multiple cracks were only observed for a small number of ruptures after dropping the balloons, but never for a rupture after piercing. Cracks initiated by piercing the membrane travelled along approximately

https://doi.org/10.1017/jfm.2014.453 Published online by Cambridge University Press

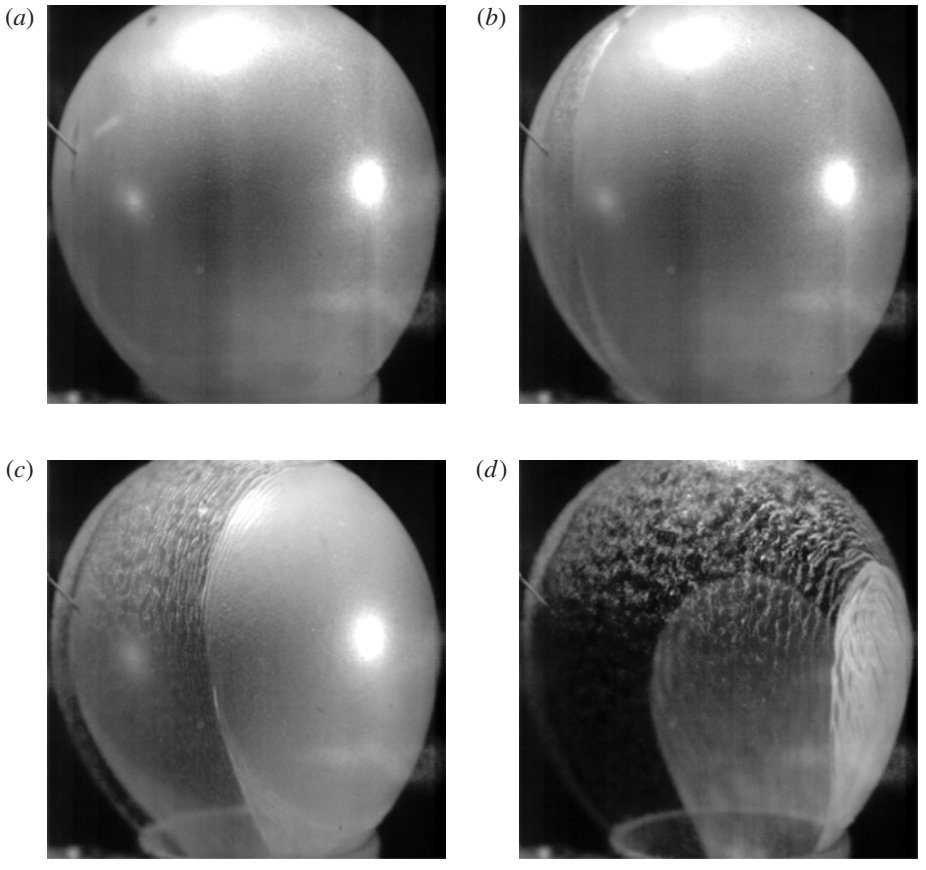


FIGURE 6. The retraction of a 130 mm water balloon membrane when underwater: (*a*) $t = 0$ ms; (*b*) $t = 0.6$ ms; (*c*) $t = 1.9$ ms; (*d*) $t = 4.3$ ms. The membrane was pricked by the pin, creating a small hole just visible in (*a*). A crack then started propagating from the hole at $t = 0$ ms. The water inside contains sodium fluorescein to aid visualisation of the interface.

straight paths initially, although it often deviated sharply once they passed through the side opposite the point at which the crack was initiated. The crack usually travelled approximately vertically, simultaneously moving from the hole created by the needle to the bottom, and from the hole to the top. This was likely a result of a lack of spherical symmetry in the balloons, as for high λ the balloons became more elongated and 'pear-like' in shape, with the curvature of the surface greater horizontally (in the azimuthal direction) than vertically (polar direction). For an elastic sheet under biaxial tension, Anderson (2004) demonstrated that the crack's path will tend to one perpendicular to the direction of the greatest tension, as this will release the greatest energy. It is well known (see Gere & Timoshenko 1997) that for a cylinder under uniform internal pressure (where the curvature is zero along the cylinder, but positive around its circumference), the tension around the circumference is twice that of the tension along its length. This suggests that greater horizontal curvature in our balloons corresponds to greater tension, explaining why the crack would tend to travel vertically.

https://doi.org/10.1017/jfm.2014.453 Published online by Cambridge University Press

The speed of the crack depended on both the extension of the membrane, and which fluids were adjacent to it. Defining the stretch λ to be the inflated radius divided by the uninflated radius, the crack speed for an air/water interface varied approximately linearly from 50 m s^{-1} for $\lambda = 3$ to 200 m s^{-1} for $\lambda = 7$. All experiments were conducted with $3 < \lambda < 7$, as below $\lambda < 3$, a crack would not propagate after piercing the membrane, and for $\lambda > 7$ there was too great a risk of the membrane rupturing spontaneously during oscillation. For a water/water interface, the speeds were slower, approximately 2/3 of those for an air/water interface for the same λ. In all cases, the propagation was consistent with 'intersonic' cracks (Petersan *et al.* 2004), travelling in excess of the shear-wave speed that is predicted to be the upper limit by classical elastic fracture theory (see Broberg 1999).

Once the crack had initiated and propagated around the membrane, the rubber either side then retracted away from the crack, due to the gradient in tension between the rest of the membrane and the stress-free faces of the crack. This retraction continued until the membrane had returned to its undeformed state (or close to it, due to viscoelastic effects), when all of its elastic tension had been relaxed. For balloons with air both inside and outside, the crack propagation speed was around three times the propagation speed of the membrane. With water present on one or both sides, the crack propagation speed was around four times the propagation speed of the membrane. The total time from initiation of the crack to the buckling of the membrane after retraction for a water balloon with air outside was typically around 4 ms, and around 5 ms for a water balloon with water outside.

The no-slip boundary condition where the membrane met the water meant that water was dragged along with the membrane as it retracted. Due to the low kinematic viscosity of water, this water accelerated by the retracting membrane was restricted to a thin boundary layer adjacent to the membrane. A typical Reynolds number for the flow within the boundary layer suggests it was within the transition region from laminar to turbulent flow. We conducted PIV experiments to examine the nature of the boundary layer either side of a strip of the balloon rubber retracting from $\lambda = 7$. Unfortunately, these experiments proved inconclusive in determining whether the boundary layer was laminar or turbulent, but the results were not inconsistent with a laminar flow. Vermorel, Vandenberghe & Villermaux (2007) used PIV to examine the nature of flow within the boundary layer for a stretched then impulsively released rubber band within glycerin of kinematic viscosity 10^{-3} m^2 s^{-1}, and found that it was laminar. Furthermore, they showed that, at position x, the flow field matched the form given by Batchelor (1967) for a flat plate initially at rest and impulsively started in motion at constant speed $U(x, t)$ when the stress wavefront passes at time $t = x/c$,

$$u(x, z, t) = U(x, t)\left[1 - \mathrm{erf}\left(\frac{z}{\sqrt{4\nu(t - x/c)}}\right)\right]. \tag{4.1}$$

It is likely, therefore, that the flow within the boundary layers either side of our impulsively released membranes was of a similar form. This then determined the flow within the wake, as discussed later.

During the retraction of the membrane, one further phenomenon of interest was observed: the development of small (around 1 mm) wavelength transverse waves near the free edge of the membrane, as shown in figure 7. They arose due to fluid loading from the water. Elsewhere on the membrane, the tension was sufficiently great, or the flow speed sufficiently low, to suppress the waves. Near the free end, though, the membrane was travelling fastest, and the tension was lowest (as it must decrease

https://doi.org/10.1017/jfm.2014.453 Published online by Cambridge University Press

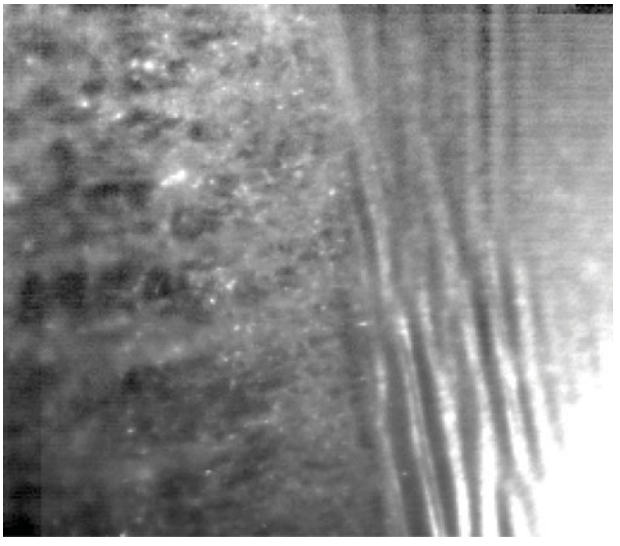


FIGURE 7. Waves seen near the free edge for a 130 mm balloon membrane underwater. The wavelength of the waves is approximately 1 mm. The image is taken from a video recorded at 75 000 f.p.s.

to zero at the free end), permitting the waves to grow. Their physical characteristics were then set by a balance between fluid loading, tension in the membrane, and bending stiffness of the membrane (due to the short wavelengths). They show great similarities to the waves seen near the end of acoustic streamers, the literature on which is reviewed by Paidoussis (2003). It is possible that their presence increased the form drag on the membrane, as suggested by the work on the drag of flapping flags by Taneda (1968), Carruthers & Filippone (2005) and Morris-Thomas & Steen (2009).

4.2. *Shear instability*

Immediately behind the retracting membrane, the fluid–fluid interface became unstable. The consequent growth of the interfacial amplitude was on a timescale and length scale less than that for the larger, later growth of the interfacial amplitude. Typically, wavelengths immediately following the retraction were around 1 mm, with full development of the instability taking around 1 ms. For an air–water interface, this interfacial growth was asymmetric (non-Boussinesq), with thin sheets or spikes of water penetrating into the air, angled toward the direction of membrane retraction. These sheets would then themselves become unstable due to capillary effects, separating into the 'spray' of droplets as seen in figure 1(*e*). For the water–water interface, the growth was symmetric and so Boussinesq, eventually causing a thin region a few millimetres thick to become turbulent.

This instability appears closely linked to that seen in the wake for uniform flow past a parallel flat plate, as discovered by Sato & Kuriki (1961), that is itself related to the wake in Bickley jets uncovered by Sato (1960). The flow within the boundary layers either side of the strip leads to a Gaussian velocity field in the wake, that is inviscidly unstable. One could regard the shear instability and waves near the free edge of the membrane as two manifestations of the same effect: in both cases, there is a thin,

https://doi.org/10.1017/jfm.2014.453 Published online by Cambridge University Press

fast-moving region surrounded by a stationary fluid, leading to disturbances growing due to centrifugal forcing. For the instability on an air/water interface, a more direct comparison may be found by considering the high-speed flow of a laminar water jet discharging from a nozzle into air, as considered by Hoyt & Taylor (1977), amongst others.

4.3. *Vorticity created by retraction*

It will be explained in § 5 that the late-time growth of the interfacial amplitude was driven by vorticity in a thin layer at the interface, and it was shown in § 3 how that vorticity was created by the preburst waves. However, the rapid retraction of the rubber led to viscous shear with the external fluid, and so also created vorticity at the interface, but with opposite signs on either side of the interface. Using the argument of Batchelor (1967), the magnitude of the circulation density γ_r on either side of the strip was simply the velocity of the strip. For a strip retracting in water, $|\gamma_r|$ was thus of the order of 30 m s^{-1}. As the vorticity passed into the wake, there was some diffusion across the line of symmetry, as the velocity profile rapidly converted from error function-like to Gaussian (see Sato & Kuriki 1961). The flapping of the membrane near its free edge also likely affected the vorticity field in the wake. Neither phenomenon, however, significantly affected either the strength or direction of the vorticity created by retraction, just the distribution.

Using the model presented in the previous section, the circulation density due to the preburst waves, γ_w, was found to be typically 1 m s^{-1}, and hence much smaller than that created by retraction of the membrane. This was no surprise, as the energy needed to stretch the membrane initially was far greater than that needed to perturb it to create the capillary-like waves. The two vorticities were also restricted to similar regions. The preburst vorticity lay in a region near the interface of thickness $\sqrt{2\nu/\omega} \approx$ 0.1 mm. If we assume that the boundary layers either side of the retracting balloons were indeed laminar, the work of Vermorel *et al.* (2007) suggests the thickness of the shear vorticity region to have been $\sqrt{4\nu t} \approx 0.2$ mm. Note, however, that for the standard crack direction, travelling from top to bottom of the balloon, the vorticities were in different orientations near the initial crack path: that created by the preburst waves lay in the θ direction, whereas that created by shear during retraction lies in the ϕ direction.

Elsewhere, however, the direction in which the membrane retracted varied, so that the orientation of the vorticity it created could coincide with that created by the preburst waves. As discussed previously, the shear instability on the interface was a consequence of the vorticity created by retraction, while the late-time instability was a consequence of the vorticity created by the preburst waves. There was therefore potential for interference between the two. An example of such interference is shown in figure 8(*a*,*b*), for an oscillation and rupture with water both inside and outside the balloon. The crack propagated down the right-hand side of the balloon, in line with the light sheet. As there was no movement of the membrane across the interface along the crack path, there was no vorticity from retraction created. Elsewhere near the crack, for both air/water and water/water cases, the vorticity that was created by the retraction did not significantly affect the late-time behaviour. In the air/water case, the vorticity was carried away from the interface by the fine spray; in the water/water case, the small length scale of the vorticity meant it dissipated far faster than for the preburst vorticity. The interface therefore evolved as a consequence of the preburst vorticity.

https://doi.org/10.1017/jfm.2014.453 Published online by Cambridge University Press

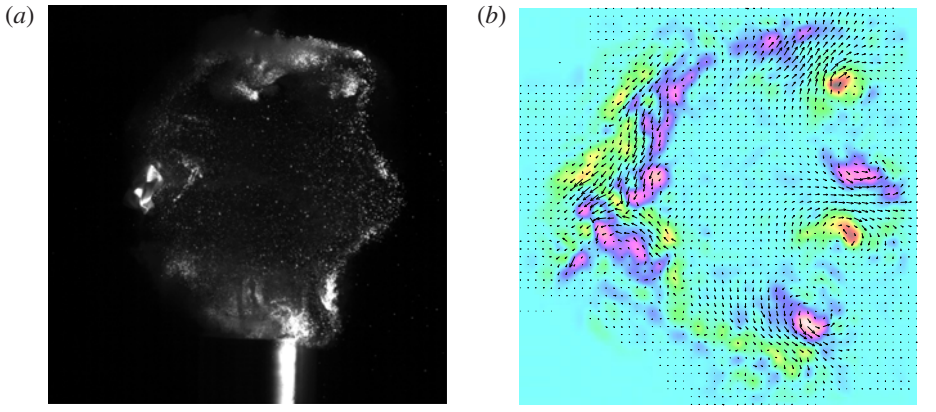


FIGURE 8. (Colour online) The full flow created by the rupture of a 130 mm balloon after being oscillated at 50 Hz underwater. The images were taken at 0.4 s after rupture. In (*a*) we show the actual experimental image, with the membrane visible half way up the image on the left-hand side. The flow was seeded with particles, so that PIV could be performed. From this PIV, the vorticity field was found, as shown in (*b*).

The situation was different on the left-hand side of the balloon, where the membrane ended up after fully retracting (as may be seen in figure 8*a*), and where the vorticity created by retraction was in the same direction as that from the preburst waves. Consequently, the vorticity created by retraction dominated the flow here post-rupture (as is clear from figure 8*b*), and so no large-scale, late-time growth of the interface was seen on that side. A similar effect was seen for all of the ruptures in water: growth according to the preburst waves was dominant on the half of the balloon nearest the initial crack path, growth according to the shear instability was dominant on the half nearest the membrane after it had fully retracted.

Note that, despite the similarity in thickness between the boundary layers created by the waves and by retraction, the length-scales of the corresponding flows were significantly different: around 0.1 mm for the shear instability, but around 10 mm for the late-time interfacial growth. This difference arose because, while the length-scale for the shear instability was set by the width of the boundary layer, that for the late-time growth was set by the length of the preburst waves. This led to a difference in momentum distribution and hence the coherence of the ensuing motion.

For ruptures in air, the development of the late-time interfacial amplitude was not affected by the retraction of the membrane, with both effects occurring on nearly the whole interface. This was because for such a large density difference across the interface, the late-time interfacial growth was not governed by the interfacial vorticity, but by momentum within the water away from the interface. This will be discussed further in the next section.

5. Late-time interfacial growth

The late-time interfacial growth observed after the bursting of a dropped or oscillated balloon was the main focus of our research, where by ‘late-time’ we refer to the interfacial growth associated with the preburst capillary waves. We are considering this to be entirely separate to the nonlinear stages of interfacial growth associated with retraction of the membrane (that occur over shorter timescales),

https://doi.org/10.1017/jfm.2014.453 Published online by Cambridge University Press

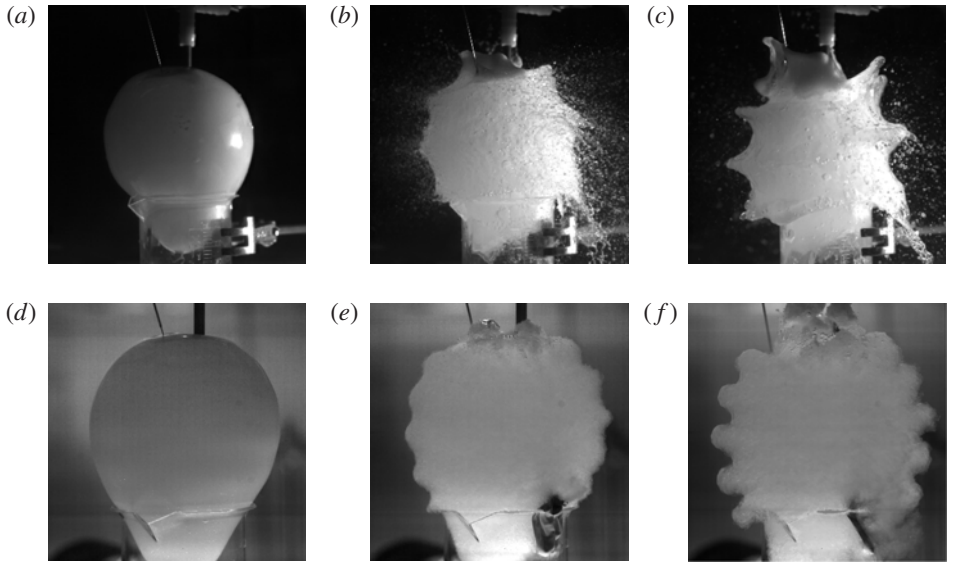


FIGURE 9. The late-time growth of the interfacial amplitude for water balloons in air (*a–c*), and water (*d–f*): (*a*) $t = 0$ ms; (*b*) $t = 17$ ms; (*c*) $t = 53$ ms; (*d*) $t = 0$ ms; (*e*) $t = 11$ ms; (*f*) $t = 72$ ms. The balloon in air was oscillated at 120 Hz prior to rupture, the balloon in water at 170 Hz prior to rupture. The water inside the balloons contained milk powder to aid visualisation.

although we acknowledge that the two phenomena may interact. In this section, our experimental observations will be described, along with our physical understanding of the process. A model will then be derived for the nonlinear growth with water on both sides of the balloon.

5.1. *Experimental results*

The late-time growth of the interfacial amplitude was discussed briefly in § 1, in relation to the bursting of water balloons dropped in air. In that case, significant growth occurred only when capillary-like waves were present on the interface at the moment of rupture. The growth developed over approximately one-twentieth of a second, with a wavelength the same as that of the waves present at the moment of rupture. The growth soon lost symmetry between the phases, taking the form of thin, circular sheets of water penetrating rapidly into the air, with wide sections of air penetrating far more slowly into the water. The tips of the thin water sheets were rounded off by surface tension, and eventually became unstable due to capillary effects and separated into droplets of water.

Examples of the late-time growth for forcibly oscillated then ruptured balloons with both air and water external to the balloon are shown in figure 9. For the forced balloons in air (figure 9*a–c*), the behaviour was nearly identical to that seen for the dropped balloons: the denser water penetrated into the air as thin 'spikes' as the air penetrated more slowly into the water as wide 'bubbles'. As we shall discuss later in § 5.3, where analogies are made to other interfacial instabilities, such asymmetry is to be expected at large Atwood numbers. The only real difference was that the growths were predominantly of a single wavenumber, whereas for a dropped balloon

https://doi.org/10.1017/jfm.2014.453 Published online by Cambridge University Press

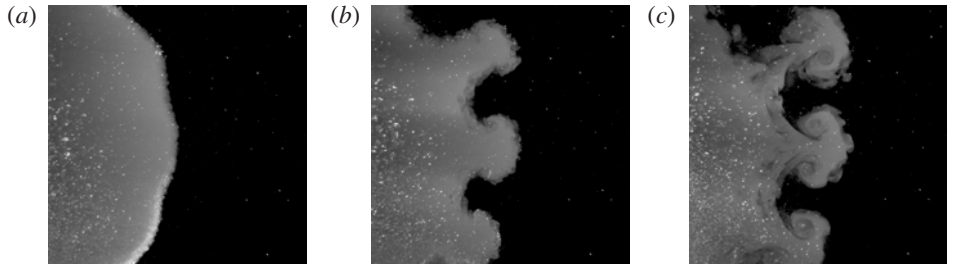


FIGURE 10. The roll-up of the interface after rupture for a 130 mm balloon oscillated at 100 Hz: (*a*) $t = 8$ ms; (*b*) $t = 81$ ms; (*c*) $t = 198$ ms. The cross-section was obtained by shining a thin light sheet through the flow, with the fluid inside containing sodium fluorescein to allow its visualisation.

they were of a range of wavenumbers. This difference arose because of the nature of the interfacial waves present on the membrane at rupture, being of only a single wavenumber set by the forcing of only a single frequency for the forced balloons, but of all wavenumbers with sufficiently large group velocity for the sudden impact of a dropped balloon.

The late-time growth from balloons forced underwater (figure 9*d–f*) shows further significant differences from the case of a dropped balloon in air. Now, the growth was symmetric between the phases inside and out, initially taking the form of growing sinusoidal perturbations. Eventually, however, the interface rolled up into vortex rings, as shown in figure 10, whose axis of symmetry is the same as for the preburst waves: the straight line from the top to the open end of the balloon ($\phi = 0,\ \pi$). The (azimuthal) vorticity within each ring was of a single sign, with the sign alternating between adjacent rings. The distance between adjacent rings was far smaller (typically around 1 mm) than the radius of each ring (typically around 50 mm). Consequently, the coupling between neighbouring rings was much stronger than the self-induced motion of each ring. The rings then propagated away from the interface in pairs, driving the interfacial growth further. Eventually, these vortex rings broke down into smaller-scale 3D structures and so stopped propagating, at which point we regarded the flow to have become fully turbulent. The total time between rupture and breakdown into turbulence was typically around 0.5 s.

In all cases, the timescale for development of the late-time amplitude growth, at least 50 ms, was significantly greater than that for phenomena associated with the retraction of the membrane, being typically of the order of 1 ms. This would suggest that the mechanism driving late-time growth was unrelated to flow created by the retraction of the membrane. This is supported by considering the energy within the flow, as shown in figure 11. This figure shows the total root-mean-squared velocity (and, hence, the square root of the kinetic energy) within one wavelength, as found using PIV experiments on a 130 mm balloon oscillated at 105 Hz then ruptured. It oscillates preburst with the same frequency as the forcing, before slowly decaying after rupture. Notably, only a small jump in the kinetic energy is observed after rupture due to the retraction of the membrane, with the energy driving the late-time growth deriving primarily from that present prior to rupture. This suggests that the retraction of the membrane does not put significant energy into the late-time flow, and so does not greatly impact the late-time growth. This supports our consideration of the late-time, large-scale growth as largely separate to the phenomena associated with retraction of the membrane.

https://doi.org/10.1017/jfm.2014.453 Published online by Cambridge University Press

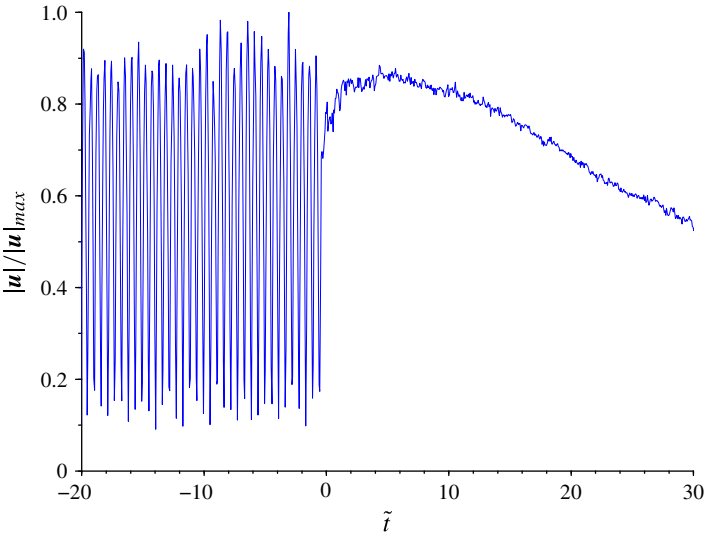


FIGURE 11. (Colour online) Root-mean-square velocity within a single wavelength, scaled against the maximum, plotted against non-dimensionalised time $\tilde{t}$ for flow within a 130 mm water balloon held underwater, and oscillated at 105 Hz prior to rupture. Rupture occurred at $\tilde{t} = 0$.

Figure 11 also indicates the importance of the phase of the waves at rupture. Preburst, the energy oscillates over a single wave-period between a minimum (when the interface was stationary but its amplitude was greatest) and a maximum (when the interface was moving fastest but its amplitude was zero). Consequently, the energy available to drive the late-time post-rupture growth would depend on the phase of the wave at which rupture occurred. Fastest interfacial growth would occur if ruptured when the interfacial amplitude was at a minimum. Should the membrane rupture at the moment of maximum interfacial amplitude, almost no interfacial growth would occur. This was a consequence of our experimental method creating standing waves on the balloon. For dropped balloons, travelling waves were created. Consequently, for a dropped balloon, the rate of interfacial growth would not depend on the phase of the wave at rupture, but the location of maximum growth would.

For balloons with water both inside and outside, we tracked the maximum interfacial displacement after rupture from the unperturbed situation for 130 mm balloons over a range of frequencies and tensions, with the results shown in figure 12. The results are non-dimensionalised as in Jacobs & Sheeley (1996), with scaled time $\tilde{t}$ given by $\Gamma k^2 t/4$, where Γ is the initial circulation within each half-wavelength and $k = k/R$ the dimensional wavenumber, and scaled displacement $\tilde{a}$ given by ka/R. As Γ was difficult to measure, the time scaling was instead determined using the equivalent relation $\tilde{t} = k\dot{a}_0 t = (1/2)ka_0\omega \sin\theta_0 t$, where ω is the angular frequency of oscillation, θ the phase of the wave at the moment of rupture, and where subscript 0 implies the value at the moment of rupture. The interface was followed by having the water inside dyed with milk powder. No measurements were taken for water balloons burst in air, as the spray caused by the retracting membrane obscured the initial linear stages of growth, while gravity dominated the nonlinear stages of growth. The membrane was ruptured so that the crack propagated in the plane perpendicular to the optical axis of the camera. The flow was then recorded at 5400 f.p.s. Using

https://doi.org/10.1017/jfm.2014.453 Published online by Cambridge University Press

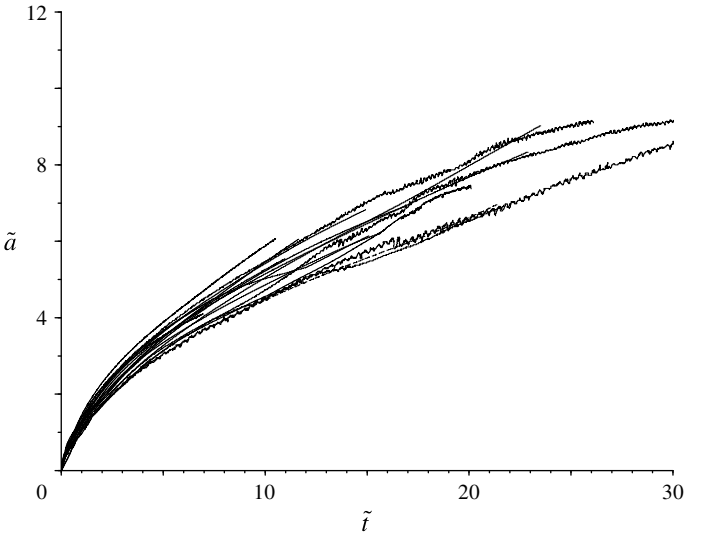


FIGURE 12. The growth rate of the interfacial amplitude for 130 mm balloons oscillated then burst with water both inside and outside. The inner fluid contained milk powder to allow easy tracking of the interface. Experiments were performed for frequencies in the range 60–180 Hz, and membrane tension between 100 and 250 N m^{-1}. The growth is shown up to $ka = 30$, when the vortex rings broke down into smaller structures as the flow became fully turbulent.

the program Digiflow, the greatest interfacial displacement was then tracked relative to its starting point.

After scaling, the results collapse down to one curve, within the margin of experimental error. The initial growth is approximately linear, before the flow decelerates at later time. Beyond $\tilde{t} = 30$, the flows lost structure and broke down into turbulence.

5.2. *Initial development of the interfacial growth*

The basic physical mechanism behind the late-time interfacial growth is explored in detail here. This mechanism is directly responsible for the behaviour in the linear stages of growth, with little difference in behaviour depending on the density ratio between the phases. This is not the case for nonlinear stages of growth, which shall be considered separately, in the next section. For the purposes of the present discussion, we shall neglect the effects of the shear-induced vorticity resulting from the retraction of the membrane, and focus instead on the vorticity associated with the preburst capillary-like waves. We shall, however, return later to consider how the retraction vorticity influences the flow.

The simplest explanation for the growth of the interfacial amplitude is that it occurs because the bursting of the balloon is a near-instantaneous removal of the restoring force (tension in the membrane) for the preburst, capillary-like waves. The flow present at the moment of rupture then continues with momentum dominant, implying a linear initial growth rate for the interfacial amplitude. Note, therefore, that this growth does not depend at all on the retraction of the membrane; the explanation is equally valid for the membrane being instantaneously removed without retracting over the interface.

https://doi.org/10.1017/jfm.2014.453 Published online by Cambridge University Press

The above argument may be made more rigorous by performing a linear stability analysis. We consider the simplest case, that of a linear, incompressible, inviscid and irrotational flow at a planar interface between two fluids. Though (as will be discussed later) such an analysis has previously been applied to study other interfacial flows, there is no evidence in the published literature of it having been applied to bursting balloons.

The quantities associated with the fluid beneath the interface will have subscript 1, those above subscript 2. This flow may be modeled using velocity potential functions ϕ_1 (below the interface) and ϕ_2 (above the interface), both of which satisfy Laplace's equation,

$$\nabla^2\phi_i = 0. \tag{5.1}$$

Assuming a 2D, Cartesian interface, the boundary conditions at the interface $z = \eta(x, t)$ are then the kinematic condition

$$\frac{\partial\eta}{\partial t} = \frac{\partial\phi_1}{\partial z}, \tag{5.2}$$

$$\frac{\partial\eta}{\partial t} = \frac{\partial\phi_2}{\partial z}, \tag{5.3}$$

and the dynamic condition

$$\rho_1\frac{\partial\phi_1}{\partial t} - \rho_2\frac{\partial\phi_2}{\partial t} + (\rho_1 - \rho_2)\eta g(t) = -\sigma(t)\frac{\partial^2\eta}{\partial x^2}, \tag{5.4}$$

where here both the gravitational acceleration g and surface tension σ are taken to be functions of time. These equations imply the potentials and interface have the form

$$\phi_1 = b(t)\mathrm{e}^{ky}\cos kx, \tag{5.5}$$

$$\phi_2 = -b(t)\mathrm{e}^{-ky}\cos kx, \tag{5.6}$$

$$\eta = a(t)\cos kx, \tag{5.7}$$

for wavenumber k and amplitudes $a(t)$ and $b(t)$. The interfacial boundary conditions then give

$$\dot{a}(t) = kb(t), \tag{5.8}$$

$$\dot{b}(t) = -\left(\frac{k^2}{\rho_1 + \rho_2}\sigma(t) + Ag(t)\right)a(t), \tag{5.9}$$

where

$$A = \frac{\rho_1 - \rho_2}{\rho_1 + \rho_2} \tag{5.10}$$

is the Atwood number. Combining these two equations leads to

$$\ddot{a}(t) = -\left(\frac{k^3}{\rho_1 + \rho_2}\sigma(t) + kAg(t)\right)a(t). \tag{5.11}$$

Different choices of $g(t)$ and $\sigma(t)$ in the above equation then determine the initial growth of the interfacial amplitude for the different situations. For the bursting

https://doi.org/10.1017/jfm.2014.453 Published online by Cambridge University Press

of a balloon, $g(t) = 0$ but $\sigma(t) = H(-t)$, where H is the Heaviside step function. Equation (5.11) thus becomes

$$\ddot{a}(t) = -\frac{k^3}{\rho_1 + \rho_2} H(-t) a(t). \tag{5.12}$$

Integrating the above equation between $-\epsilon$ and t (where both ϵ and t are positive) gives

$$\dot{a}(t) - \dot{a}(-\epsilon) = -\frac{k^3}{\rho_1 + \rho_2} \int_{-\epsilon}^{0} a(t)\,\mathrm{d}t. \tag{5.13}$$

Taking the limit $\epsilon \to 0$ therefore implies

$$\dot{a}(t) = \lim_{\epsilon \to 0} \dot{a}(-\epsilon) = \dot{a}_0, \tag{5.14}$$

where $\dot{a}_0$ is the normal velocity of the interface at that moment of rupture. This implies, as argued above, that the initial interfacial growth after rupture will be linear, going at the velocity of the interface at the moment of rupture. This linearity was supported by experimental measurements of the interfacial growth for water/water ruptures, as shown in figure 12. The initial gradient is 1, as the scalings used are equivalent to $\tilde{t} = (k/R)\dot{a}_0 t$ and $\tilde{a} = (k/R)a$. This linear behaviour persists until approximately $\tilde{t} = 2$, when it starts to decelerate as the flow becomes nonlinear. This theory also predicts that the interface retains its initial sinusoidal shape in the initial linear stage of growth, and consequently that the shape remains symmetric (and so independent of the relative densities of the two fluids). This was indeed the case, as seen in figure 9(*b*,*e*). Note that (5.14) also implies a difference in linear growth based on the nature of the waves: if travelling waves are present (as for a dropped balloon), the initial growth rate will be the same whenever the balloon bursts, although the location of fastest growth will change; with standing waves present (as for our forced balloons), the location of fastest growth will be fixed, but the initial growth rate will depend on the phase of the preburst wave at which the balloon ruptures.

The above analysis has been conducted without specifying the densities of the fluids either side of the interface. Consequently, while our focus is on the cases with water inside the balloon (due to the relative ease of conducting such experiments, and the fact that compressibility of the fluids may be neglected in such cases), the same mechanism for growth will still occur with air inside and water outside, provided there are waves on the balloon at the moment of rupture. The same would also be true for air both sides of the membrane, although then the greater mass of the membrane in comparison with the fluids either side would mean that the dispersion relation of the preburst waves would differ from those given in § 3.

Note that a better model of our balloons would arguably be with $\sigma(t) = H(-t) - H(t_* - t)$ for some $t_* < 0$, representing the application of a tensile restoring force to the interface for a finite time before rupture. However, the analysis for $t > 0$ would be identical to the semi-infinite case considered above, as all that matters is the behaviour at $t = 0$, not what has happened before.

Through this linear stability analysis, it can be seen how the growth of the interfacial amplitude due to the bursting of a balloon may be related to other phenomena, most notably the Rayleigh–Taylor instability (RTI) and the Richtmyer–Meshkov instability (RMI). RTI, as discussed in Acheson (1990), occurs when a density interface is subjected to a destabilising acceleration that is constant in time,

https://doi.org/10.1017/jfm.2014.453 Published online by Cambridge University Press

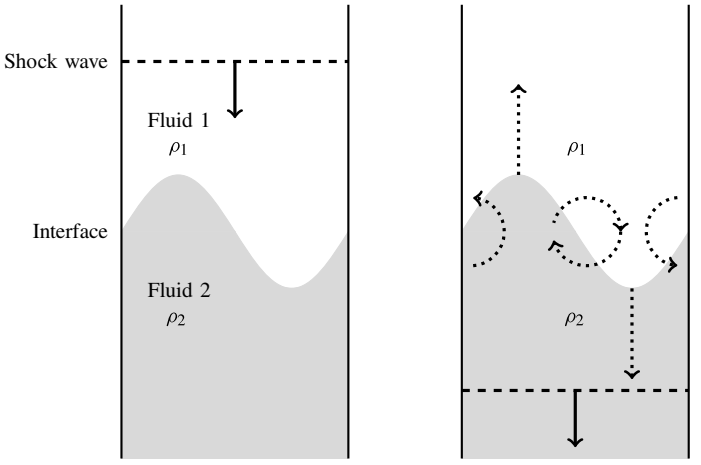


FIGURE 13. Diagram illustrating the appearance of RMI after shock passes through a perturbed interface, as Baroclinic vorticity generation on the surface leads to growth in the amplitude of the interface. In this example $\rho_2 > \rho_1$, while the dotted lines represent the direction of flow.

leading to exponential growth of the interfacial amplitude. RMI, as introduced by Richtmyer (1960) and Meshkov (1969), is closely related to RTI. It may occur on any interface between two compressible fluids of differing density; unlike RTI, reversing the ratio of densities only changes the phase of the interfacial amplitude growth. This growth is classically understood to develop as a result of the passing of a shock wave through a perturbed interface. The perturbations on this interface may lead to a misalignment of the density and pressure gradients at the surface, causing the instability to develop. As can be seen from the $\nabla\rho \times \nabla p$ term of the (inviscid) vorticity equation

$$\frac{\mathrm{D}\boldsymbol{\omega}}{\mathrm{D}t} = \frac{1}{\rho^2}\left(\nabla\rho \times \nabla p\right) + \left(\boldsymbol{\omega}\cdot\nabla\right)\boldsymbol{u} - \boldsymbol{\omega}(\nabla\cdot\boldsymbol{u}), \tag{5.15}$$

this misalignment leads to the deposition of vorticity upon the interface that leads to growth in the amplitude of perturbations (see figure 13).

Richtmyer (1960) derived an approximate linear relation for the initial growth of a single mode due to this instability,

$$\dot{\eta} = Ak\Delta V\eta_0, \tag{5.16}$$

where k is the (dimensional) wavenumber of the interfacial wave, ΔV is the difference in the surface velocity immediately before and after the shock passes, and η_0 is the initial amplitude of that disturbance.

A large number of experimental studies have also been conducted into both compressible and incompressible RMI. Of particular interest are the incompressible experiments of Jacobs & Sheeley (1996), Niederhaus & Jacobs (2003) and Chapman & Jacobs (2006), who conducted a detailed investigation into RMI created by a sled containing two miscible liquids falling onto a spring. Their results for the linear stages of interfacial growth show good agreement with (5.16).

https://doi.org/10.1017/jfm.2014.453 Published online by Cambridge University Press

It should be noted that we have referred to this effect as an instability as that is how it is commonly referred to in the literature. However, RMI is not a true instability: the initial growth from infinitesimal perturbations is not exponential in time (as for RTI), but linear, and the interface only experiences a positive acceleration momentarily, after which it decelerates. It is, therefore, best regarded as a mechanism for interfacial growth, not as an interfacial instability. Consequently, we shall often refer to the Richtmyer–Meshkov mechanism (RMM), by which we mean the physics responsible for the flow that is usually called the RMI. Any reference to RMI will refer to the growth of a shock-accelerated interface. By these definitions, RMM is more general than RMI, and may applied to situations that do not include shock acceleration.

Furthermore, when we do refer to RMI we refer to the definition of Jacobs & Sheeley (1996), that it is the impulsive acceleration of a density interface. Impulsive accelerations of the whole flow may only occur on an interface between incompressible fluids. For compressible fluids, impulsive acceleration is given by a shock wave passing through the interface. Other authors, including (Velikovich *et al.* 2000), define RMI to be when a shock wave passes through a interface, thus excluding the possibility of RMI for incompressible flow (in which shocks cannot occur). Despite this, the incompressible case is still referred to by Velikovich *et al.* (2000) as 'Richtmyer–Meshkov-like', as it does feature the same deposition of initial localized vorticity at the interface that causes the growth.

The connection between RTI, RMM and growth of the interface due to a bursting balloon becomes clear by repeating the previous analysis for the initial growth rate. This was first done by Taylor (1950) for RTI, for an interface with gravitational acceleration: $g(t) = g\,\mathrm{sgn}(-t)$ and $\sigma(t) = 0$. Equation (5.11) thus becomes

$$\ddot{a}(t) = -kAga(t), \tag{5.17}$$

and so the initial interfacial growth is exponential in time for $t > 0$. This is distinct from the balloon and RMI cases, as the interface is being constantly accelerated throughout growth of the interfacial amplitude. In the other two, no acceleration is applied once growth has begun.

The linear stability analysis for RMI was first considered by Richtmyer (1960), where it was modelled as the impulsive limit of RTI. Although the author was concerned with the compressible case, his model is actually most relevant to the incompressible case. The acceleration on the interface is $g = \Delta V\delta(t)$ (where ΔV is the difference in normal velocity either side of the shock) and $\sigma(t) = 0$. Equation (5.11) thus becomes

$$\ddot{a}(t) = -kA\Delta V\delta(t)a(t). \tag{5.18}$$

Integrating up once gives the growth rate for $t > 0$ as

$$\dot{a}(t) = \dot{a}(0) - kA\Delta Va(0), \tag{5.19}$$

showing that the initial interfacial growth is linear in time, its speed being constant as for the bursting balloon case. Note that as we are considering the incompressible, impulsively accelerated case, $a(0)$ is well defined; this is not the case for the compressible, shock-accelerated case.

The connection between bursting balloons and RMI through initial linear growth is more than coincidence. In fact, the flow is identical between an impulsively accelerated interface after the acceleration, and the balloon interface once the

https://doi.org/10.1017/jfm.2014.453 Published online by Cambridge University Press

membrane has ruptured. This is best seen by considering vorticity. It is well known that the basic driving mechanism for RMI is the baroclinic deposition of vorticity at the interface by the impulsive acceleration. The relevant version of the vorticity equation, including the baroclinic term, is

$$\frac{\mathrm{D}\omega}{\mathrm{D}t} = \frac{1}{\rho^2}\nabla\rho \times \nabla p. \tag{5.20}$$

When the interface is impulsively accelerated, ∇p will be normal to it. If there are any perturbations to the interface, $\nabla\rho$ will not be normal to the interface. The density and pressure gradients will therefore be misaligned, leading to the creation of vorticity. In the inviscid limit, this vorticity will be restricted to an infinitely thin sheet at the interface. The flow associated with this vorticity will then cause the interfacial amplitude to increase. This is true wherever the vorticity actually is, even for an air/water interface where the vorticity is in the air. We may therefore refer to RMM as the growth of interfacial amplitude due to the presence of an interfacial vortex sheet whose sign alters along the interface, for which there is no mechanism to significantly deposit further vorticity.

For the interfacial growth of a bursting balloon, it was explained in § 3 how the preburst waves create vorticity localised near the interface, that in the limit of small viscosity may be approximated by a vortex sheet, with the sign of the vorticity changing along the sheet. Once the balloon bursts, this vortex sheet is left at the interface. The situation is now identical to that for an interface has been impulsively accelerated: the flow implied by the vortex sheet causes the interfacial amplitude to grow. The growth is therefore linear, as for RMI.

It should be noted that, in our above argument for the interfacial growth in the balloon case, the fact that the interfacial waves were capillary waves was not important. We would therefore also expect interfacial growth to occur if the restoring force for gravity waves was present for a finite time before being instantaneously removed. The initial growth rate would then be given by (5.11) with $g(t) = gH(-t)$ and $\sigma(t) = 0$, and hence $\dot{a}(t) = \dot{a}(0)$. Such a situation could be created by forming gravity waves on a tray of water in the absence of surface tension, before the tray is released into free fall.

Up to this point in the literature, RMM has typically been regarded as a consequence of the impulsive, or instantaneous, acceleration of an interface. Through our experiments on bursting water balloons, we have shown that this definition is arguably imprecise: the growth of the interfacial amplitude is a consequence of the instantaneous removal of the acceleration (or equivalently, the instantaneous removal of the restoring force for waves). It does not matter whether that restoring force is applied instantaneously (RMI) or for a finite time (as for a balloon). Indeed, it is noticeable that in our previous linear stability analysis for bursting balloons that the growth of the interface is independent of the time for which the acceleration was applied to the interface preburst. After removal of the acceleration, the flow evolves according to that present at the moment of removal, the interfacial amplitude growing linearly in time due to the vorticity present at the interface. For balloon bursts with standing waves on the interface, the interfacial growth does, of course, depend on the exact time of rupture: the phase of the waves at the moment of rupture will determine the normal velocity of the interface, and therefore the initial growth rate. It does not, however, depend on how long the waves have been present.

The only difference between a balloon burst and RMI is in how the vorticity is created. For RMI (and gravity waves), it is baroclinically generated at the interface.

https://doi.org/10.1017/jfm.2014.453 Published online by Cambridge University Press

Consequently, no growth will occur when the densities of the two fluids are the same, when $A = 0$. This is a clear distinction with the balloon case, where the interfacial waves are generated by a form of surface tension. The creation of these waves, and hence the interfacial vorticity and consequent interfacial growth after their removal, will therefore occur even when $A = 0$.

In summary, the growth of interfacial amplitude after a balloon bursts is closely related to the RMI. In RMI, vorticity at a density interface produced by impulsive acceleration leads to growth of the interfacial amplitude at constant speed. Our experiments on bursting water balloons, however, show that vorticity produced at an interface by capillary-like waves can also lead to growth of the interfacial amplitude, if and when the restoring force for those waves is instantaneously removed. In fact, similar to how Kelvin–Helmholtz instability may be simply regarded as the instability of a vortex sheet of constant vorticity, RMM may be regarded as the instability of a vortex sheet of sinusoidal sections of alternating sign. Under such a definition, the rupture of a balloon would indeed be a example of RMM.

We must remark here that the presence of the vorticity associated with the retraction of the membrane complicated matters. The linear growth was unaffected by the high-wavenumber perturbation of the retraction instability, but it is likely that the nonlinear growth was influenced. Such dependence on the details of the initial conditions has been seen previously for RTI by Rollin & Andrews (2013) and for RMI by Balasubramanian, Orlicz & Prestridge (2013).

The linear stability analysis presented in this subsection is only valid when the interfacial amplitude was small in comparison with the wavelengths of the perturbation. Once they were of a similar order, the analysis may no longer be accurate. In the nonlinear stages of growth, unlike the linear stages, the relative densities of the two fluids became important. Once again, this closely mirrors the behaviour of both RTI and RMM for the equivalent density ratio.

5.3. *Nonlinear air/water interface*

For the air/water interface, $A \approx 1$ and thus the relative density difference between the fluids was large. As seen in figure 14 (and in figure 9*a–c*), the non-Boussinesq nature of the flow became important, as the interfacial growth lost symmetry between the phases. Thin sheets of water penetrated into the air, while thicker intrusions of air moved into the water at a far slower rate. This behaviour closely mirrored that of RTI and RMI at high Atwood number (see, for example, Buttler *et al.* 2012), where the wide intrusions of the less dense fluid are referred to as bubbles, and the thin sheets of denser fluid are referred to as spikes. Notably, and unlike for the water/water case below, no roll-up of the interface occurred. The precise reason for this difference in behaviour to lower Atwood numbers is unclear, although it was likely a combination of two factors. One was surface tension, as any roll-up would have led to a large increase in the area of the air/water interface. The other factor was the large density difference between the phases, that led to a mismatch in momentum between the phases. The vortex sheet was therefore stretched out along the interface as it rapidly grew in area, so that it could not form the tight spirals typical of roll-up.

We explained in § 3 how the presence of the membrane changed the structure of the interfacial vorticity, when compared with that for capillary waves on a pure fluid–fluid interface. In both cases, the instantaneous removal of the restoring force led to the late-time growth of the interfacial amplitude. However, while the interfacial vorticity may be approximated in all cases by an infinitely thin sheet in the inviscid limit,

https://doi.org/10.1017/jfm.2014.453 Published online by Cambridge University Press

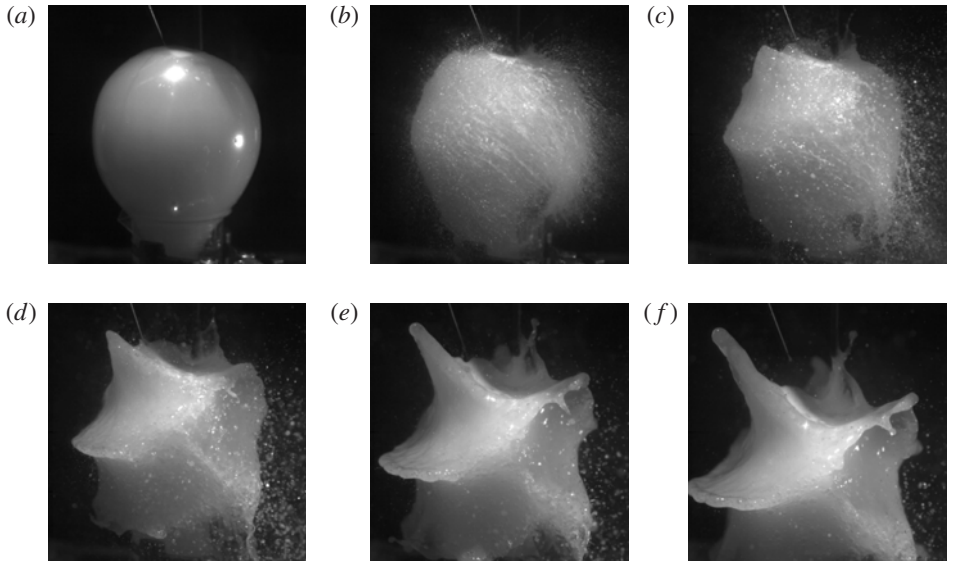


FIGURE 14. The late-time growth of the interfacial amplitude for a water-filled 130 mm balloon oscillated at 80 Hz prior to rupture: (*a*) $t = 0$ ms; (*b*) $t = 7$ ms; (*c*) $t = 16$ ms; (*d*) $t = 36$ ms; (*e*) $t = 67$ ms; (*f*) $t = 94$ ms. The water inside the balloons contained milk powder to aid visualisation. The instability is only clearly visible on the left side of the balloon, as that was where the crack propagated. On the right side, vorticity created by the retracting membrane dominated the flow instead. At the later times, the effect of gravity can clearly be seen, causing the entirety of the water to slump down.

physically that is not possible, with the actual location of the vorticity depending on the nature of the interface. For the water/water case when $A = 0$ this did not matter, as there was no difference between the phases. However, for the air/water case when $A \approx 1$, it may have mattered. For a true air/water free surface as for RMI, whether impulsively accelerated or accelerated for a finite time, and whether due to gravity or capillary forces, the vorticity would be concentrated in the less-dense air. For a membrane-covered interface, the vorticity would be split, with approximately half in the air and half in the water. This could, potentially, have led to differences in the late-time behaviour. As noted above, the vorticity associated with retraction could also have affected the late-time behaviour. However, the structure of the instability displayed in figure 14 for a bursting balloon did match that seen for RTI and RMI for $A \approx 1$, indicating that the location of the vorticity was not significant in determining the general form of the interfacial growth. At such low viscosities, the approximation of the vorticity as a sheet at the interface was still accurate, suggesting that its exact location did not matter. This does, however, raise the possibility of the flow structure being significantly different if the fluid within the balloon is not water but something far more viscous. To date, no experiments have been undertaken in this more viscous regime.

The location of the interfacial vorticity, if not important in determining the overall structure of the interfacial growth, could still have impacted the growth rate. Unfortunately, it was not possible for us to accurately measure the growth rate of the bubbles and spikes in the nonlinear regime, as at such late-times gravity and surface tension came to dominate the flow. This caused the water to slump down

https://doi.org/10.1017/jfm.2014.453 Published online by Cambridge University Press

and the spikes to break up into droplets, introducing further nonlinear complications to the motion of the fluids, and meaning the interfacial growths no longer travelled along simple, straight paths.

5.4. *Nonlinear water/water interface*

For the water/water interface, when $A = 0$, the behaviour was distinctly different. Now there was no mismatch of momentum, the flow was Boussinesq and the growth was essentially symmetric, as the interfacial vorticity rolled up into discrete vortex rings of alternating sign on lines of constant latitude. Similar behaviour (although with straight vortex tubes instead of vortex rings) has been noted before for both RTI and RMI at low Atwood numbers, including by Jacobs & Sheeley (1996) for incompressible RMI on a planar interface.

The connection between the interfacial growth after the bursting of a balloon and RMI was made in § 5.2. For RMI, a variety of models have been proposed for the growth rate of the individual bubbles and spikes, although there is no one universally accepted model; a detailed review of the models available for planar geometry is given in Brouillette (2002). A significant amount of numerical work has also been carried out on RMI on curved (Glimm, Grove & Zhang 2000) and spherical (Dutt *et al.* 2004) surfaces, but these studies did not provide predictions for the growth of the interfacial amplitude. At later times, when the flow becomes fully turbulent, the growth of the interfacial amplitude is believed to follow a power law that may depend sensitively on the details of the initial conditions (Balasubramanian *et al.* 2013) and on the vorticity introduced by retraction of the membrane, although that regime is beyond the scope of this paper.

Distinct from most previous studies relating to RMM, however, the vortex rings here were of varying radius and circulation due to the spherical shape of the interface. Consequently, mutual interaction between these rings caused them to separate into pairs and propagate away from the interface. As the vortex rings were a mix of both fluids, they took the interface with them, and so were the primary driving mechanism behind the nonlinear interfacial growth at very late times. This process is clearly seen in figure 15 through the use of PIV on an oscillated water balloon rupturing underwater. Eventually, these vortex rings broke down into smaller scales as the flow became fully turbulent. This typically occurred before a scaled time $\tilde{t} = 30$. Note that this behaviour was only observed on the half of the interface closest to the initial path of crack propagation. Elsewhere, vorticity created by the retracting membrane dominated the behaviour, causing the flow to become turbulent almost immediately after rupture ($\tilde{t} < 1$). This also meant that the vortex rings were not fully closed. However, enough of the interface did roll up into the rings for them to be the dominant structures in the flow on one side of the balloon at late times.

Growth rates for the water/water case were shown in figure 12. In particular, they show that the growth decelerated as it entered the nonlinear regime. However, this deceleration did not last for long, with the growth becoming approximately linear once again, albeit at a slower speed than immediately after rupture. This was different from the behaviour of incompressible RMI at low Atwood numbers studied by Jacobs & Sheeley (1996), who found that the interfacial amplitude grew like $\log(k\dot{a}_0 t)$ at late times (as will be discussed in the following section). However, as stated previously, their experiments were conducted on flat interfaces, whereas ours were conducted on spherical interfaces. It therefore seems that the unperturbed shape of the interface played a key role in determining the nonlinear interfacial growth rate.

https://doi.org/10.1017/jfm.2014.453 Published online by Cambridge University Press

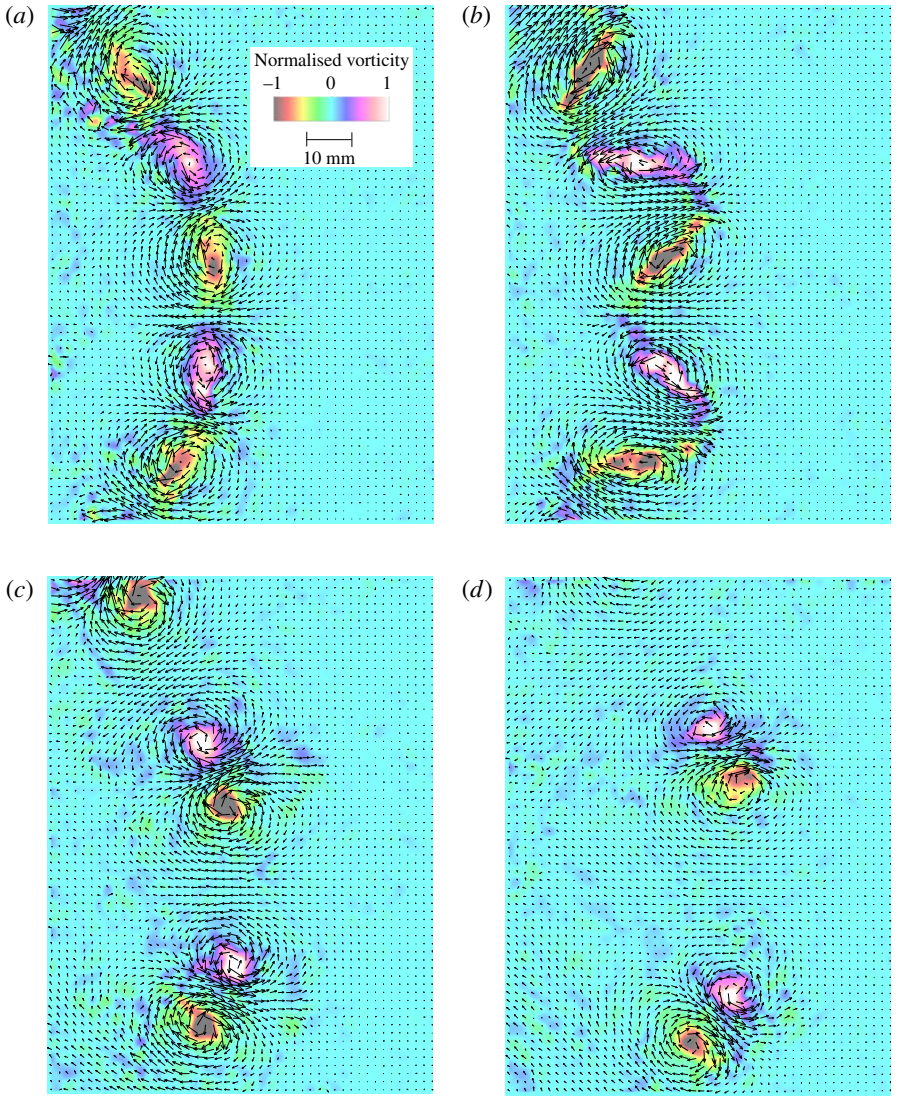


FIGURE 15. (Colour online) The results of PIV on a cross-section of the flow created by a 130 mm balloon forcibly oscillated at 105 Hz before being ruptured by a pin: (*a*) $t = 0$ ms; (*b*) $t = 20$ ms; (*c*) $t = 117$ ms; (*d*) $t = 221$ ms. The arrows represent the velocity field and the colours represent the vorticity, with purple positive, cyan zero and red negative. Prior to rupture, the vorticity was restricted to a narrow region near the interface. Post-rupture, the vorticity rolled up into discrete rings. These rings then separated into pairs of opposite sign, and propagated away from the initial interface. Image (*d*) shows two such pairs.

6. Vortex model for nonlinear growth when $A = 0$

Jacobs & Sheeley (1996), in their work on RMI in the low-Atwood-number regime, developed a theory to match their experimental results that was referred to as the 'vortex model'. This model was based on the idea that the late-time behaviour was dominated by the interfacial vorticity. As they were considering a 2D horizontal

https://doi.org/10.1017/jfm.2014.453 Published online by Cambridge University Press

(although perturbed) interface, the initial distribution of circulation density γ given by linear theory was

$$\gamma = -2\dot{a}\sin kx \tag{6.1}$$

for $-\infty < x < \infty$. The model assumed that the sinusoidal distribution of vorticity present on the interface at time $t = 0$, when the shock passed through the interface, instantaneously rolled up into discrete vortices. As the initial distribution of vorticity was assumed to extend to plus and minus infinity, all of the vortices would remain in their initial position. They could thus find an analytical expression for the stream function of the flow, and thus for the growth of the maximum amplitude of the interface. The expression for the stream function found was

$$\psi = \frac{\Gamma}{4\pi}\ln\frac{\cosh ky + \sin kx}{\cosh ky - \sin kx}, \tag{6.2}$$

for vortices of circulation $\pm\Gamma$ separated by a distance π/k, k being the wavenumber of the interfacial perturbation at $t = 0$. The consequent expression for the growth of the amplitude $a(t)$ was

$$a(t) = \frac{1}{k}\sinh^{-1}\left(\frac{2}{\pi}k\dot{a}_{0+}t + \sinh ka_0\right). \tag{6.3}$$

Consequently, as $t \to \infty$, $a \sim \ln t$ and $\dot{a} \sim 1/t$. This expression, when matched with experimental data, showed a good qualitative agreement but predicted growth rates below those observed experimentally. As the authors noted, as the growth rate is reduced by the coalescence of vorticity, which occurs gradually, it is reasonable to expect the vortex model to always yield a lower growth rate than that of experimental measurements.

A similar model was derived by Likhachev & Jacobs (2005) to model bubble and spike growth on a low Atwood number interface. They did this by assuming the oppositely-signed vortices were not equally spaced along the interface at $t = 0$. Consequently, the vortices did not remain stationary, but propagated away from the initial interface at a constant velocity, consequently affecting the late-time growth rate of the interface. As $t \to \infty$, they showed that the interface speed would approach that of the vortices.

As discussed previously, and much like incompressible RMI, the late-time interfacial growth after a balloon bursts is also driven by a vortex sheet at the interface. For bursting balloons, however, this is in a different geometrical configuration: instead of a 2D interface, upon bursting of the balloon the vorticity is initially restricted to a spherical interface, but quickly coalesces into vortex rings. These vortex rings are of alternating sign and centred on the symmetry axis of the balloon's forcing. The initial self-induced motion of the vortex rings means that a pairing process occurs, as each core has an initial net velocity towards one of its neighbours. Once the initial circular symmetry is broken, each core also gains a velocity normal to the initial interface due to mutual induction with its 'partner'. At later times, this mutual induction comes to dominate, and the two vortices behave similar to a pair of translating vortices of equal strength but opposite sign (as discussed by Batchelor 1967, p. 531).

The rings were of finite core radius that decreased as the rings expanded. However, by Kelvin's circulation theorem, we expected their circulation to remain constant as they propagated away from the interface. This is clearly demonstrated in figure 16 for the initial stages of growth, where $\tilde{t} < 10$. However, later on, as the vortex rings

https://doi.org/10.1017/jfm.2014.453 Published online by Cambridge University Press

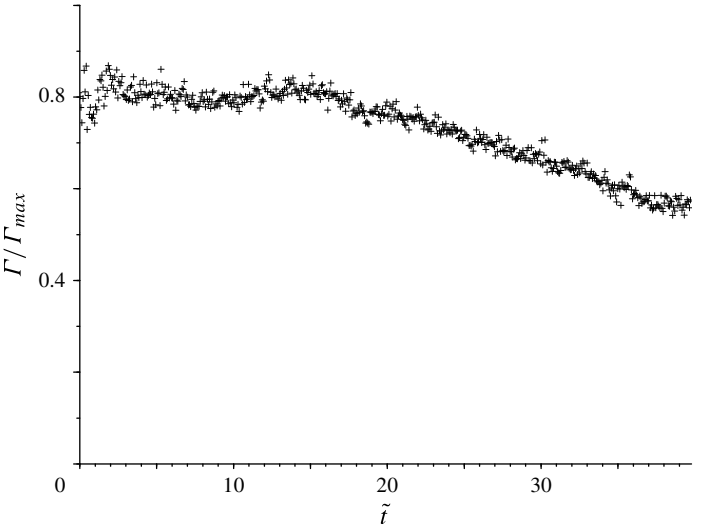


FIGURE 16. The normalised total circulation within one half wavelength (equivalently, one vortex ring) after rupture of a 130 mm balloon forced at 105 Hz, plotted against time.

approached one another to form pairs, the vorticity was annihilated at the centreline between each pair of rings, and the circulation decreased linearly. We estimate the error bars for figure 16 to be ± 0.05.

To model the nonlinear stages of interfacial growth when $A = 0$, we therefore extend the work of Jacobs & Sheeley (1996) and Likhachev & Jacobs (2005) by assuming the interfacial vorticity concentrated at the interface at the moment of burst instantaneously rolls up into discrete vortex rings. Due to axisymmetry, we simplify the problem by considering a 2D cross-section of the system, where each vortex ring is replaced by a pair of oppositely signed point vortices, as shown in figure 17. For a single vortex ring, it is known that such an approximation does not give the correct translation speed for the ring, as it does not account for the curvature of the ring (see Saffman 1992). However, as the distance between adjacent rings is far smaller than the diameter of each ring, we expect the point vortex approximation to be reasonable, with any correction for the curvature of each ring to be insignificant. Most importantly, the self-induced motion of each ring would be in the same direction as that implied by the point vortex model. It is further assumed that each ring has the same strength circulation. Although this assumption was shown to be technically incorrect in § 3, it is reasonable for high-wavenumber bursts near the balloon's equator, as for all our experimental measurements, where $k > 6$. The assumption that this circulation is constant over time is also used. Note that in figure 17, should rupture occur half a period later, the sign of each point vortex would change. Consequently different pairs would form, although the flow would be otherwise unchanged.

In summary, we shall attempt to model the late-time interfacial growth by assuming that the interfacial vorticity instantaneously rolls up into vortex rings. These rings form a system equivalent to an even number (as each ring contributes two vortices) of point vortices of equal, constant strength circulation but alternating sign arranged in a circle in a 2D plane.

https://doi.org/10.1017/jfm.2014.453 Published online by Cambridge University Press

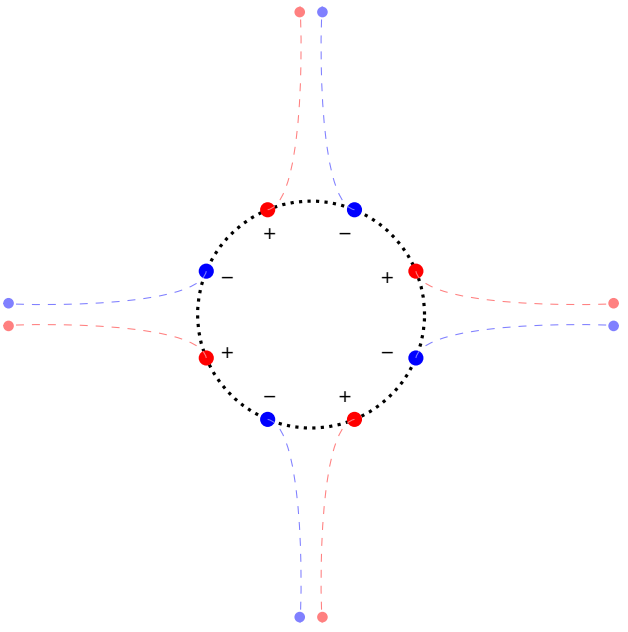


FIGURE 17. (Colour online) The approximate motion of eight vortices of alternating sign initially arranged on a circle. They separate off into adjacent pairs that head off to infinity together.

We first wish to determine the motion of the vortices, from which we may then determine the stream function and hence the overall flow field. For such a system of n vortices, we thus have $2n$ unknowns to find, the x and y coordinates of each vortex. However, we may use the inherent symmetry of the initial conditions (and subsequent motion) to reduce the problem to one of finding the x and y coordinates of just one vortex. By symmetry, the motion of all of the other vortices will then be same, only rotated, reflected, or both. In fact, this situation is analogous to a single vortex in a wedge, as its motion may be solved using the method of images, leading to a consideration of the situation we have here. This situation was first considered by Greenhill (1878), who found the polar equation of the motion. However, he did not solve for the motion in terms of time, which we require. We thus rederive the equations of motion, and solve for both radius and polar angle in terms of time.

We work in circular polar coordinates with radial coordinate r and polar angle ζ, taking $\zeta = 0$ along the positive x-axis. The vortices are initially distributed on the circle $r = r_0$ at positions $\zeta = (\pi(2j-1))/n$ for $j = 1, \ldots, n$, with circulation

$$\Gamma_j = (-1)^{j+1}\Gamma \tag{6.4}$$

for some positive constant Γ. The vortices then separate into pairs whose motion is symmetric across the lines $\zeta = 4\pi m/n$ for $m = 1, \ldots, n/2$.

We assume, as is usual, that the motion of each vortex is solely due to the sum of the velocity fields induced by the other vortices. The stream function ψ_j created by a vortex of strength Γ_j at position $z_j = r_j e^{i\zeta}$ in the complex plane is (Batchelor 1967),

$$\psi_j = -\frac{\Gamma_j}{2\pi} \ln |z - z_j|, \tag{6.5}$$

https://doi.org/10.1017/jfm.2014.453 Published online by Cambridge University Press

meaning that the stream function for the flow at vortex 1, $\tilde{\psi}$, is

$$\tilde{\psi} = -\frac{\Gamma}{2\pi}\left(\sum_{j=1}^{(n/2)-1} \ln|z - z_{2j+1}| - \sum_{j=1}^{n/2} \ln|z - z_{2j}|\right). \tag{6.6}$$

6.1. *Equations of motion of a vortex*

Taking the position of vortex 1 to be $(a(t),\ \phi(t))$ (functions of t alone), with consequent complex position $z_1 = a(t)\mathrm{e}^{\mathrm{i}\phi(t)}$, symmetry then gives the complex positions of the other vortices as

$$z_{2j} = a\mathrm{e}^{\mathrm{i}(\tilde{\phi}_j - \phi)}, \tag{6.7}$$

$$z_{2j+1} = a\mathrm{e}^{\mathrm{i}(\tilde{\phi}_j + \phi)}, \tag{6.8}$$

$$\tilde{\phi}_j = \frac{4\pi j}{n}. \tag{6.9}$$

We may thus rewrite (6.6) as

$$\begin{aligned}\tilde{\psi} \;=\; -\frac{\Gamma}{4\pi}\Bigg(&-2\ln a + \ln\left[1 + \left(\frac{r}{a}\right)^n - 2\left(\frac{r}{a}\right)^{n/2}\cos\frac{n}{2}(\zeta - \phi)\right] \\ &- \ln\left[1 + \left(\frac{r}{a}\right)^n - 2\left(\frac{r}{a}\right)^{n/2}\cos\frac{n}{2}(\zeta + \phi)\right] \\ &- \ln\left[1 + \left(\frac{r}{a}\right)^2 - 2\left(\frac{r}{a}\right)\cos(\zeta - \phi)\right]\Bigg).\end{aligned} \tag{6.10}$$

From the stream function we may find the velocity $\boldsymbol{v} = (v_r,\ v_\zeta)$ of vortex 1 using the relations

$$v_r = \left[\frac{1}{r}\frac{\partial\tilde{\psi}}{\partial\zeta}\right]_{(a,\phi)}, \quad v_\zeta = \left[-\frac{\partial\tilde{\psi}}{\partial r}\right]_{(a,\phi)}. \tag{6.11a,b}$$

Doing so leads to the two equations

$$\dot{a} = \frac{\Gamma}{4\pi a}\left(\frac{n}{2}\right)\cot\frac{n\phi}{2}, \tag{6.12}$$

$$\dot{\phi} = -\frac{\Gamma}{4\pi a^2}. \tag{6.13}$$

To solve for the motion of vortex 1, we divide (6.12) by (6.13) to give

$$\frac{\dot{a}}{\dot{\phi}} = \frac{\mathrm{d}a}{\mathrm{d}\phi} = -a\left(\frac{n}{2}\right)\cot\frac{n\phi}{2}. \tag{6.14}$$

Together with the initial condition

$$a\left(\frac{\pi}{n}\right) = r_0, \tag{6.15}$$

this leads to

$$a(\phi) = r_0\csc\left(\frac{n\phi}{2}\right). \tag{6.16}$$

https://doi.org/10.1017/jfm.2014.453 Published online by Cambridge University Press

This is the equation given by Greenhill (1878). Substituting (6.16) into (6.13) gives

$$\dot{\phi} = -\frac{\Gamma}{4\pi r_0^2} \sin^2\left(\frac{n\phi}{2}\right). \tag{6.17}$$

Solving this together with the initial condition $\phi(0) = \pi/n$, we get ϕ as a function of t,

$$\phi(t) = \frac{2}{n} \cot^{-1}\left(\frac{\Gamma n}{8\pi r_0^2} t\right). \tag{6.18}$$

Equation (6.12) then becomes

$$\dot{a} = \frac{\Gamma}{4\pi a} \frac{n}{2} \left(\frac{\Gamma n}{4\pi r_0^2} t\right). \tag{6.19}$$

Using the initial condition $a(0) = r_0$, we find

$$a(t) = r_0 \left[1 + \left(\frac{\Gamma n}{8\pi r_0^2} t\right)^2\right]^{1/2}. \tag{6.20}$$

We can easily deduce from (6.18) and (6.20) that as $t \to \infty$, $a \to \infty$ and $\phi \to 0$ as we would expect. However, what is of greater interest is the distance between the vortices in each pair and their velocity as $t \to \infty$. If we denote the distance between the vortices as $l(t)$ and their displacement along their centreline as $x(t)$, the distance $l(t)$ is given by

$$l(t) = 2\,a \sin(\phi) = 2\,r_0 \frac{\sin(\phi)}{\sin\left(\frac{n\phi}{2}\right)}. \tag{6.21}$$

As we know already that as $t \to \infty$, $\phi \to 0$, we see (using L'Hopital's rule)

$$\lim_{t\to\infty} l(t) = \frac{4r_0}{n}. \tag{6.22}$$

The velocity of the vortices as $t \to \infty$ may be directly inferred from the fact that the late-time motion is dominated by mutual interaction between each pair of point vortices. Their asymptotic velocity is thus

$$\begin{aligned} \lim_{t\to\infty} \dot{x}(t) &= \frac{\Gamma}{2\pi \lim_{t\to\infty} l(t)} \\ &= \frac{\Gamma n}{8\pi r_0}. \end{aligned} \tag{6.23}$$

We expect the interface to travel at the same velocity as the vortices at late times, just as for Likhachev & Jacobs (2005), thus approximately following the relation

$$r(t) = \frac{\Gamma n}{8\pi r_0} t + C, \tag{6.24}$$

for some constant C that depends on k. It will therefore be linear in time, in contrast to the behaviour for a flat interface found by Jacobs & Sheeley (1996), where the

https://doi.org/10.1017/jfm.2014.453 Published online by Cambridge University Press

growth is asymptotically logarithmic. We define the dimensional wavelength of the disturbance on the interface at time $t = 0$ as

$$\lambda = \frac{2\pi}{\frac{n}{2}} r_0 = \frac{4\pi r_0}{n}, \tag{6.25}$$

and hence the dimensional wavenumber as

$$k = \frac{2\pi}{\lambda} = \frac{n}{2r_0}. \tag{6.26}$$

Equation (6.24) then becomes

$$kr(t) = \frac{\Gamma k^2}{4\pi} t + kC. \tag{6.27}$$

Taking the scalings as used in Jacobs & Sheeley (1996) as before, we write

$$\tilde{t} = \frac{\Gamma k^2}{4} t, \tag{6.28}$$

$$\tilde{r} = kr, \tag{6.29}$$

leading to the equation

$$\tilde{r}(\tilde{t}) = \frac{1}{\pi}\tilde{t} + \tilde{C}. \tag{6.30}$$

We shall compare this with the experimental measurements shortly, but first we extend the analysis to find a theoretical prediction for the flow at any point, and thus find a prediction for the interfacial displacement valid for all of $0 < t < \infty$. This is necessary, as most of our experiments only permit tracking of the interface, whose displacement differed significantly from that of the driving vortex rings in the early stages of interfacial growth.

The stream function for the flow away from any of the vortex cores is

$$\begin{aligned}\psi \;=\; & -\frac{\Gamma}{4\pi}\left(-2\ln a + \ln\left[1 + \left(\frac{r}{a}\right)^n - 2\left(\frac{r}{a}\right)^{n/2}\cos\frac{n}{2}(\zeta - \phi)\right]\right. \\ & \left. - \ln\left[1 + \left(\frac{r}{a}\right)^n - 2\left(\frac{r}{a}\right)^{n/2}\cos\frac{n}{2}(\zeta + \phi)\right]\right),\end{aligned} \tag{6.31}$$

where a and ϕ are as derived previously. This is the stream function used previously but with the addition of the term representing vortex 1.

The maximum displacement of the interface in the direction of increasing r will occur on the centreline between two vortices in a pair. We consider the motion along the line $\zeta = 0$ so as to simplify the analysis. The angular velocity of any point along line $\zeta = 0$ is necessarily zero, due to the symmetry of the problem. Consequently we need only consider the radial component, given by

$$\begin{aligned}\dot{r} \;&=\; \left[\frac{1}{r}\frac{\partial\psi}{\partial\phi}\right]_{(r,0)} \\ &=\; \frac{\Gamma}{2\pi r}\left[\frac{n\left(\frac{r}{a}\right)^{n/2}\sin\frac{n}{2}\phi}{1 + \left(\frac{r}{a}\right)^n - 2\left(\frac{r}{a}\right)^{n/2}\cos\frac{n}{2}\phi}\right].\end{aligned} \tag{6.32}$$

https://doi.org/10.1017/jfm.2014.453 Published online by Cambridge University Press

Using (6.26), we now define

$$\begin{aligned}\hat{a}(t) &= \frac{a(t)}{r_0} \\ &= \left(1+\left(\frac{\Gamma k^2}{2\pi n}t\right)^2\right)^{1/2}.\end{aligned} \tag{6.33}$$

Using this definition, together with (6.16), allows (6.32) to be written as

$$\dot{r} = \frac{\Gamma k}{\pi \hat{a}^2}\frac{\left(\dfrac{2k\,r}{n\hat{a}}\right)^{(n/2)-1}}{1+\left(\dfrac{2k\,r}{n\hat{a}}\right)^n - 2\left(\dfrac{2k\,r}{n\hat{a}}\right)^{n/2}\left(1-\dfrac{1}{\hat{a}^2}\right)^{1/2}}. \tag{6.34}$$

Together with the initial condition

$$r(0) = r_0 = \frac{n}{2k}. \tag{6.35}$$

Equation (6.34) may be solved numerically to give a theoretical prediction for the maximum interface displacement as a function of time t. Note that we initially assumed that Γ was positive; taking instead Γ negative, (6.34) and (6.35) describe the evolution in time of the minimum interface displacement, as then the vortices separate off into different pairs.

To check (6.34), we can also find an analytical solution to it in the case of $n \to \infty$ while k remains constant and finite. As

$$k = \frac{n}{2r_0} \tag{6.36}$$

this means we are taking r_0 to infinity too. Physically, this corresponds to an infinite row of vortices at a distance

$$\lambda = \frac{2\pi}{k} \tag{6.37}$$

apart, exactly the situation considered by Jacobs & Sheeley (1996).

We define the (scaled) function

$$\begin{aligned}\tilde{x}(\tilde{t}) &= k\,(r(t) - r_0) \\ &= \tilde{r}(\tilde{t}) - \frac{n}{2}.\end{aligned} \tag{6.38}$$

It follows that

$$\tilde{x}(0) = 0. \tag{6.39}$$

As $n \to \infty$, $\hat{a} \to 1$ so that (6.34) becomes

$$\frac{\mathrm{d}\tilde{x}}{\mathrm{d}\tilde{t}} = \frac{4}{\pi}\left(\frac{1}{1+\dfrac{2\tilde{x}}{n}}\right)\frac{\left[\left(1+\dfrac{2\tilde{x}}{n}\right)^n\right]^{1/2}}{1+\left(1+\dfrac{2\tilde{x}}{n}\right)^n}. \tag{6.40}$$

https://doi.org/10.1017/jfm.2014.453 Published online by Cambridge University Press

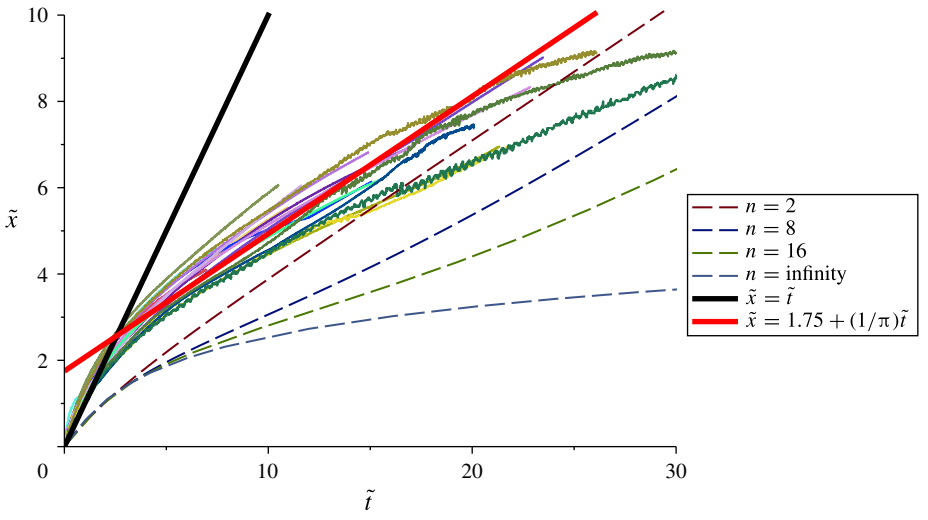


FIGURE 18. (Colour online) The interfacial displacement $\tilde{x}$ plotted against time $\tilde{t}$. Shown are theoretical predictions for $n = 2$, $n = 8$, $n = 16$ and $n = \infty$ (the model of Jacobs & Sheeley 1996), together with the experimental data, and the lines $\tilde{x} = \tilde{t}$ (black) and $\tilde{x} = 1.75 + (1/\pi)\tilde{t}$ (red).

In the limit $n \to \infty$ keeping t and $\tilde{x}$ fixed, equation (6.40) becomes

$$\begin{aligned} \frac{\mathrm{d}\tilde{x}}{\mathrm{d}\tilde{t}} &= \frac{4}{\pi}\frac{\mathrm{e}^{\tilde{x}}}{1+\mathrm{e}^{2\tilde{x}}} \\ &= \frac{2}{\pi}\frac{1}{\cosh\tilde{x}}, \end{aligned} \tag{6.41}$$

the same equation found by Jacobs & Sheeley (1996). They go on to solve this equation, which in scaled coordinates becomes

$$\tilde{x}(t) = \sinh^{-1}\left(\frac{2}{\pi}\tilde{t} + \sinh\tilde{x}_0\right). \tag{6.42}$$

It is notable that this solution behaves like $\ln(2t)$ at infinity, whereas all solutions for finite n behave like $(1/\pi)\tilde{t}$ at infinity.

6.2. *Comparison with experiments*

Theoretical solutions for $n = 2$, 8, 16 and ∞ plotted on figure 18, along with our experimental data and the lines $\tilde{x} = \tilde{t}$ and $\tilde{x} = (1/\pi)\tilde{t} + 1.75$. The solutions for $2 < n < \infty$ lie between those for $n = 2$ and $n = \infty$, eventually tending to parallel with $(1/\pi)\tilde{t}$.

When compared with this experimental data, the theoretical predictions appear to have the correct shape, but lie below the experimental data. This was also observed by Jacobs & Sheeley (1996) (with the initial gradient out by the same factor of $2/\pi$) and is due to the different initial distributions of vorticity. With the vorticity initially distributed sinusoidally, 2D potential theory predicts the initial velocity to be greater than that for point vortices by the factor $2/\pi$. Rescaling the theoretical predictions so

https://doi.org/10.1017/jfm.2014.453 Published online by Cambridge University Press

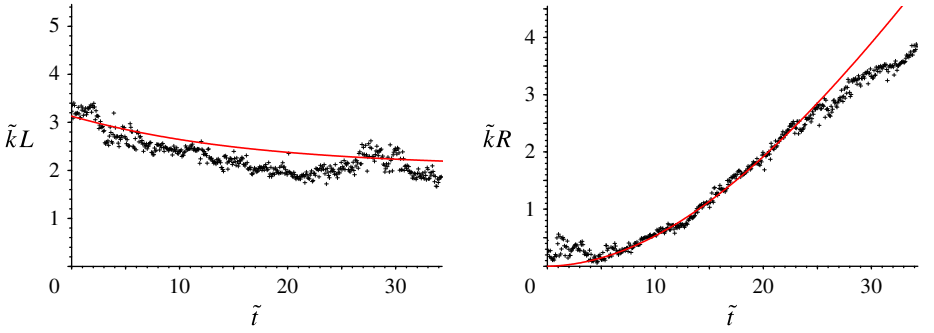


FIGURE 19. (Colour online) The behaviour over time of (*a*) the distance between two vortices L and (*b*) their displacement R from the interface at the moment of rupture, for a 130 mm balloon forced at 50 Hz with water both inside and outside the balloon. The black marks denote the experimental data, while the (red online) line gives the theoretical prediction. Due to the time taken for the vorticity to roll-up, time $\tilde{t}=0$ is not the moment of rupture but chosen to be 5.3 after to give the best fit to the data.

that the initial velocity is the same provides a better match at early times. However, this rescaling is equivalent to increasing the vorticity, and thus doing so means the theoretical models now over-estimate the final, constant late-time velocity.

Also plotted in figure 18 is the best fit for the late-time asymptotic behaviour $\tilde{a}=\tilde{C}+(1/\pi)\tilde{t}$ with $\tilde{C}=1.75$. The constant C was determined using a least-squares best fit on the data lying in $10<\tilde{t}<30$. This compares well with the value found by Jacobs & Sheeley (1996), $\tilde{C}=2$. This best fit asymptotic behaviour provides a good fit with the data between $\tilde{t}=5$ and $\tilde{t}=20$. However, it does appear to overestimate the asymptotic growth rate, $\dot{\tilde{a}}=1/\pi$. The reason for this will be discussed later, but is a combination of the initial interfacial vorticity being an overestimate for the circulation within the rings, and the rings approaching so closely that the modeling of them as point vortices is no longer valid.

No attempt is made to compare our data to the other models for nonlinear incompressible RMI detailed by Niederhaus & Jacobs (2003), as all are only applicable for flat interfaces. On such interfaces, the vortex patches remain stationary under their mutually induced action, whereas for our axisymmetric spherical interface they do not. Comparing the models therefore makes little sense, save for noting that the asymptotic growth rate for $A=0$ on a flat interface is proportional to $1/t$, decaying over all time, whereas for a spherical interface it tends to a constant value, and so does not decay.

To show that it is indeed the movement of the vortex rings that drives the later growth, we have used PIV to track the rings after the rupture of a balloon on a water/water interface. Two rings are followed, with the location of the rings determined by the positions of minimum and maximum vorticity. Results for the distance between the rings L and their displacement from the initial interface $R-R_0$ over time is given in figure 19, along with theoretical predictions, for which the circulation of each vortex was chosen to be the circulation within the half-wavelength at the moment of rupture. Both L and $R-R_0$ agree well with theory, when adjusted to allow for the time taken for the vorticity to roll up into discrete rings. In particular, they show that both the distance between the rings and their speed approaches the correct asymptotic value for $\tilde{t}<25$.

https://doi.org/10.1017/jfm.2014.453 Published online by Cambridge University Press

The comparison shown in both figures 18 and 19 is far from perfect. Part of this discrepancy will be down to experimental error. However, our simple point vortex model above also makes several assumptions that are not completely valid. The first is that the circulation within each ring is equal. As discussed in § 3, and predicted by linear theory, this was not true. However, the difference in circulation between neighbouring rings was small near $\phi = \pi/2$ for large wavenumbers, exactly the conditions under which the measurements were taken in all our experiments. More relevantly, we also assumed that all of the vorticity initially near the interface was rolled up into the vortex rings that then propagated away from the interface. However, our PIV experiments suggested that up to 15 % of the initial vorticity was left behind by the vortex rings as they propagated away from the interface, thus reducing the circulation and, hence, the propagation speed of the rings. The vorticity that is left behind may also have influenced the flow directly. Our model also assumed that each ring could be accurately modelled as a point vortex, so that the shape of the core of each ring could be neglected. It is debatable whether this approximation was valid at any time; we would argue that the rings were initially far enough apart that this was a reasonable assumption, as it was for the 2D model of Jacobs & Sheeley (1996). However, unlike in Jacobs & Sheeley (1996), here our vortices move closer together at late times. It can clearly be seen in figure 15 how the distance between the rings decreases dramatically as they propagate away from the initial interface, to the point where each core has deformed to become elliptical under the influence of its partner. Although the stretching of the ring counteracts this effect at later times, figure 15 demonstrates that it was important for at least part of the motion. It is clear that when such behaviour occurs, it is no longer accurate to model each ring as a point vortex, or thin ring. It is then well known (see Saffman 1992) that a pair of oppositely signed vortex patches travels slower than a pair of point vortices of the same total separation and the same distance between the centres. We note, however, that accounting for the finite core sizes would not change the overall structure of the flow.

One final source of inaccuracy only affects the behaviour at very late times. Our model predicts the propagation speed of the vortex rings to approach a finite non-zero value as $\tilde{t} \to \infty$, something that should still be true (if for an slightly different speed) even for the sources of inaccuracy discussed in the previous paragraph. What is observed beyond $\tilde{t} = 25$, however, is that the speed of the vortices decreases away from the theoretical asymptotic value. The reason for this that the circulation within each ring decays over time once it gets close enough to its partner, an effect not present in our model as it neglects viscosity. This is clearly displayed in figure 16 with data from an experiment, where the circulation remains constant while the initial vortex sheet rolls up, before it then decreases linearly until the flow breaks down. Such a linear decay has been noted before, including by Stanaway, Cantwell & Spalart (1988) for colliding viscous vortex rings, and by Archer, Thomas & Coleman (2010) for a simulation of a vortex ring colliding with a stationary free surface (thus simulating the collision of two vortex rings due to the free slip condition at the interface, and the image of the vortex ring in that interface). Both state that this loss of circulation is down to vorticity annihilation at the mid-line between the vortex rings, as the positive vorticity on one side diffuses over the centre line between the rings, where it meets and cancels with the negative vorticity from the other side. Entrainment of fluid from outside the rings may also increase the separation and reduce the vorticity of the cores.

https://doi.org/10.1017/jfm.2014.453 Published online by Cambridge University Press

7. Conclusion

We have considered the behaviour of the water within a water-filled balloon when dropped from a great enough height such that it ruptures due to the impact. As this situation was difficult to study quantitatively, we used an alternative experimental method in which the balloons were held stationary then forced at a single frequency, before being rupture by a pin. Both the dropped and oscillated balloons displayed the same three significant stages. The first was the appearance of waves on the balloon preburst, for which the restoring force was tension within the rubber membrane. For the dropped balloon, they were travelling waves of a range of frequencies, while for the oscillated balloons, they were standing waves of only a single frequency. We showed how low-viscosity linear theory models the waves well, the waves being similar in nature to capillary waves on a water droplet, particularly with regards to their oscillation frequency. However, the elasticity of the membrane was shown to affect both the decay rate of the waves and the location of the interfacial vorticity they create; the effect of this change in vorticity on the post-rupture behaviour was not explored, although was likely small for fluids of such low viscosity as water and air. Should the balloon rupture, one (or potentially more in the case of a dropped balloon) cracks propagated through the membrane, from which the membrane retracted. The flow in the wake behind the retracting membrane was similar to the that in the wake behind a flat plate parallel to the flow, and so a shear instability soon developed. For a water-filled balloon burst in air, the nonlinear growth of this instability manifested as a 'spray' of water droplets ejected from the surface. Finally, if there were tension-driven waves present on the membrane at the moment of rupture, a later, larger-scale growth of the interfacial amplitude was seen. Whatever the fluids either side of the membrane, the initial growth was driven by the momentum of the fluids due to the preburst wave motion. The travelling waves on a dropped balloon meant that growth always occurred at the same rate, although the location of maximum growth depended on the phase of the wave at rupture. For the standing waves on the oscillated balloons, the location of maximum growth was known, but the growth-rate depended on the phase of the wave at rupture. We explained how the physical mechanism driving this growth may be regarded as the same as that behind shock-driven RMI. For bursts with air external to the balloon, momentum continued to drive the growth as the interfacial amplitude became nonlinear, until gravity caused the whole flow to slump down. However, unlike shock-driven RMI, significant interfacial growth could occur with no density difference across the interface. This we examined with water on both sides of the membrane; then, the nonlinear stages of growth were driven by the vorticity left at the interface by the preburst waves. The vorticity within each half-wavelength rolled up into a vortex ring, the mutual interaction between the rings then causing them to separate into pairs and propagate outwards from the initial interface. We derived a point vortex model for this nonlinear growth, similar to that of Jacobs & Sheeley (1996) for RMI on a flat interface at low Atwood numbers. Our model predicted the interfacial growth rate to approach a constant non-zero value as $t \to \infty$. This was in contrast to a flat interface, where the growth rate decays logarithmically as $t \to \infty$. The predicted asymptotic growth-rate matched well with the results of our experiments, until the effects of turbulence, secondary instabilities and diffusion became significant, and the vortex rings broke down into smaller-scale structures. Indeed, the quality of this match was surprising, demonstrating that the vorticity introduced by the retraction process had an insignificant effect on the late-time growth when compared with the vorticity due to the waves on the interface at $t = 0$.

https://doi.org/10.1017/jfm.2014.453 Published online by Cambridge University Press

The connection between the late-time interfacial growth after a water balloon bursts and RMM is the main result of this paper. Despite the inherent difficulty in performing well-controlled experiments with a retracting membrane, we believe this work suggests a new way to study the RMI experimentally, using a method requiring less energy and specialized knowledge than the standard shock-driven techniques.

Acknowledgement

This research was supported by EPSRC studentship grant number EP/P504120/1.

Supplementary movies

Supplementary movies are available at http://dx.doi.org/10.1017/jfm.2014.453.

REFERENCES

ACHESON, D. J. 1990 *Elementary Fluid Dynamics*. Oxford University Press.

ANDERSON, T. L. 2004 *Fracture Mechanics: Fundamentals and Applications*, 3rd edn. Taylor and Francis.

ARCHER, P. J., THOMAS, T. G. & COLEMAN, G. N. 2010 The instability of a vortex ring impinging on a free surface. *J. Fluid Mech.* **642**, 79–94.

BALASUBRAMANIAN, S., ORLICZ, G. C. & PRESTRIDGE, K. P. 2013 Experimental study of initial condition dependence on turbulent mixing in shock-accelerated Richtmyer–Meshkov fluid layers. *J. Turbul.* **14** (3), 170–196.

BATCHELOR, G. K. 1967 *An Introduction to Fluid Dynamics*. Cambridge University Press.

BROBERG, K. B. 1999 *Cracks and Fracture*. Academic Press.

BROUILLETTE, M. 2002 The Richtmyer–Meshkov instability. *Annu. Rev. Fluid Mech.* **34**, 445–468.

BUTTLER, W. T., ORÓ, D. M., PRESTON, D. L., MIKAELIAN, K. O., CHERNE, F. J., HIXSON, R. S., MARIAM, F. G., MORRIS, C., STONE, J. B., TERRONES, G. & TUPA, D. 2012 Unstable Richtmyer–Meshkov growth of solid and liquid metals in vacuum. *J. Fluid Mech.* **703**, 60–84.

CARRUTHERS, A. & FILIPPONE, A. 2005 Aerodynamic drag of streamers and flags. *J. Aircraft* **42** (4), 976–982.

CHAPMAN, P. R. & JACOBS, J. W. 2006 Experiments on the three-dimensional incompressible Richtmyer–Meshkov instability. *Phys. Fluids* **18**, 074101.

CHRISTENSEN, K. H. 2005 Transient and steady drift currents in waves damped by surfactants. *Phys. Fluids* **17**, 042102.

CRAIK, A. D. D. 1985 *Wave Interactions and Fluid Flows*. Cambridge University Press.

DUTTA, S., GLIMM, J., GROVE, J. W., SHARP, D. & ZHANG, Y. 2004 Spherical Richtmyer–Meshkov instability for axisymmetric flow. *Maths Comput. Simul.* **65**, 417–430.

GERE, J. M. & TIMOSHENKO, S. P. 1997 *Mechanics of Materials*, 4th edn. PWS.

GLIMM, J., GROVE, J. W. & ZHANG, Y. 2000 Three dimensional axisymmetric simulations of fluid instabilities in curved geometry. *Adv. Fluid Mech* **26**, 643–652.

GREENHILL, A. G. 1878 Plane vortex motion. *Q. J. Pure Appl. Maths* **15**, 10–29.

HOYT, J. W. & TAYLOR, J. J. 1977 Waves on water jets. *J. Fluid Mech.* **83** (1), 119–127.

JACOBS, J. W. & SHEELEY, J. M. 1996 Experimental study of incompressible Richtmyer–Meshkov instability. *Phys. Fluids* **8**, 405–415.

LAMB, H. 1932 *Hydrodynamics*. Cambridge University Press.

LIKHACHEV, O. A. & JACOBS, J. W. 2005 A vortex model for Richtmyer–Meshkov instability accounting for finite Atwood number. *Phys. Fluids* **17**, 031704.

LUCASSEN-REYNDERS, E. H. & LUCASSEN, J. 1969 Properties of capillary waves. *Adv. Colloid Interface Sci.* **2**, 347–395.

MARK, J. E. 2009 *Polymer Data Handbook*, 2nd edn. Oxford University Press.

MESHKOV, E. E. 1969 Instability of the interface of two gases accelerated by a shock wave. *Izv. Akad. Nauk SSSR Mekh. Zhidk. Gaza* **4**, 151–157.

https://doi.org/10.1017/jfm.2014.453 Published online by Cambridge University Press

MILLER, C. A. & SCRIVEN, L. E. 1968 The oscillations of a fluid droplet immersed in another fluid. *J. Fluid Mech.* **32**, 417–425.

MORRIS-THOMAS, M. T. & STEEN, S. 2009 Experiments on the stability and drag of a flexible sheet under in-plane tension in uniform flow. *J. Fluids Struct.* **25** (5), 815–830.

MULLINS, L. 1969 Softening of rubber by deformation. *Rubber Chem. Technol.* **42**, 339–362.

NIEDERHAUS, C. E. & JACOBS, J. W. 2003 Experimental study of the Richtmyer–Meshkov instability of incompressible fluids. *J. Fluid Mech.* **485**, 243–277.

PAIDOUSSIS, M. P. 2003 *Fluid Structure Interactions: Slender Structures and Axial Flow*, vol. vol. 2. Elsevier Academic Press.

PETERSAN, P. J., DEEGAN, R. D., MARDER, M. & SWINNEY, H. L. 2004 Cracks in rubber under tension exceed the shear wave speed. *Phys. Rev. Lett.* **93**, 015504.

RAYLEIGH, L. 1879 On the capillary phenomena of jets. *Proc. R. Soc. Lond.* **29**, 71–97.

RICHARD, D. & QUERE, D. 2000 Bouncing water drops. *Europhys. Lett.* **50**, 769–775.

RICHTMYER, R. D. 1960 Taylor instability in shock acceleration of compressible fluids. *Commun. Pure Appl. Maths* **13**, 297–319.

ROLLIN, B. & ANDREWS, M. J. 2013 On generating initial conditions for turbulence models: the case of Rayleigh–Taylor instability turbulent mixing. *J. Turbul.* **14** (3), 77–106.

SAFFMAN, P. G. 1992 *Vortex Dynamics*. Cambridge University Press.

SATO, H. 1960 The stability and transition of a two-dimensional jet. *J. Fluid Mech.* **7** (01), 53–80.

SATO, H. & KURIKI, K. 1961 The mechanism of transition in the wake of a thin flat plate placed parallel to a uniform flow. *J. Fluid Mech.* **11** (Pt 3), 321–352.

STANAWAY, S. K., CANTWELL, B. J. & SPALART, P. R. 1988 A numerical study of viscous vortex rings using a spectral method. *NASA STI/Recon Tech. Rep. N* 89, 23820.

TANEDA, S. 1968 Waving motions of flags. *J. Phys. Soc. Japan* **24** (2), 392–401.

TAYLOR, G. 1950 The instability of liquid surfaces when accelerated in a direction perpendicular to their planes. I. *Proc. R. Soc. Lond.* A **201** (1065), 192–196.

VELIKOVICH, A. L., DAHLBURG, J. P., SCHMITT, A. J., GARDNER, J. H., PHILLIPS, L., COCHRAN, F. L., CHONG, Y. K., DIMONTE, G. & METZLER, N. 2000 Richtmyer–Meshkov-like instabilities and early-time perturbation growth in laser targets and *Z*-pinch loads. *Phys. Plasmas* **7**, 1662–1671.

VERMOREL, R., VANDENBERGHE, N. & VILLERMAUX, E. 2007 Rubber band recoil. *Proc. R. Soc.* A **463**, 641–658.

https://doi.org/10.1017/jfm.2014.453 Published online by Cambridge University Press